Bioactive Materials 42 (2024) 32–51

Contents lists available at ScienceDirect

Bioactive Materials

journal homepage: www.keaipublishing.com/en/journals/bioactive-materials

Dissolvable microneedle-based wound dressing transdermally and continuously delivers anti-inflammatory and pro-angiogenic exosomes for diabetic wound treatment

Yanpeng Cao [a,1], Bei Chen [a,b,c,e,1], Qixing Liu [a], Yiyang Mao [b,c], Yusheng He [a], Xiaoren Liu [a], Xin Zhao [a], Yaowu Chen [a], Xiying Li [a], Yabei Li [a], Liang Liu [a], Chengwu Guo [a], Shiyu Liu [a], Fenghua Tan [a], Hongbin Lu [c,d,e], Jun Liu [a,**], Can Chen [b,c,e,2,*]

[a] Department of Limbs (Foot and Hand) Microsurgery, Chenzhou No.1 People's Hospital, The First Clinical Medical College Affiliated to Southern Medical University, Chenzhou, Hunan, China
[b] Department of Orthopedics, Xiangya Hospital, Central South University, Changsha, Hunan, China
[c] National Clinical Research Center for Geriatric Disorders, Xiangya Hospital, Central South University, Changsha, Hunan, China
[d] Department of Sports Medicine, Xiangya Hospital, Central South University Changsha, Hunan, China
[e] Key Laboratory of Organ Injury, Aging and Regenerative Medicine of Hunan Province, Changsha, Hunan, China

ARTICLE INFO

Keywords:
Acellular dermal matrix
Diabetic wound
Exosomes
Microneedle
Transdermal delivery

ABSTRACT

Due to overactive inflammation and hindered angiogenesis, self-healing of diabetic wounds (DW) remains challenging in the clinic. Platelet-derived exosomes (PLT-Exos), a novel exosome capable of anti-inflammation and pro-angiogenesis, show great potential in DW treatment. However, previous administration of exosomes into skin wounds is topical daub or intradermal injection, which cannot intradermally deliver PLT-Exos into the dermis layer, thus impeding its long-term efficacy in anti-inflammation and pro-angiogenesis. Herein, a dissolvable microneedle-based wound dressing (PLT-Exos@ADMMA-MN) was developed for transdermal and long-term delivery of PLT-Exos. Firstly, a photo-crosslinking methacrylated acellular dermal matrix-based hydrogel (ADMMA-GEL), showing physiochemical tailorability, fast-gelling performance, excellent biocompatibility, and pro-angiogenic capacities, was synthesized as a base material of our dressing. For endowing the dressing with anti-inflammation and pro-angiogenesis, PLT-Exos were encapsulated into ADMMA-GEL with a minimum effective concentration determined by our in-vitro experiments. Then, in-vitro results show that this dressing exhibits excellent properties in anti-inflammation and pro-angiogenesis. Lastly, in-vivo experiments showed that this dressing could continuously and transdermally deliver PLT-Exos into skin wounds to switch local macrophage into M2 phenotype while stimulating neovascularization, thus proving a low-inflammatory and pro-angiogenic microenvironment for DW healing. Collectively, this study provides a novel wound dressing capable of suppressing inflammation and stimulating vascularization for DW treatment.

1. Introduction

The global prevalence of adult diabetes will increase to 7.7 % by 2030, and diabetes-associated complications seriously threaten the health of patients and increase medical costs and mortality [1–3]. Diabetic wounds (DW), a major complication of diabetes mellitus, happen in about 15–25 % of diabetic patients [4,5]. Pathologically, the DW consistently exists pro-inflammatory M1 macrophages accompanied by excessive production of reactive oxygen species (ROS) and pro-inflammatory cytokines, which induces chronic inflammation and hinders adequate angiogenesis, thereby significantly restricting the delivery of oxygen and nutrients to the wound site as well as the removal of

Peer review under responsibility of KeAi Communications Co., Ltd.
* Corresponding author. Department of Orthopaedics, Xiangya Hospital, Central South University, No 87 of Xiangya Road, Changsha, 410008, China
** Corresponding author. Chenzhou No.1 People's Hospital, No.102 of Luojiajing Road, Beihu District, Chenzhou, 423000, China.
E-mail addresses: liujunheliyun@163.com (J. Liu), chencanwow@foxmail.com, chencan@csu.edu.cn (C. Chen).
[1] These authors have contributed equally to this work and share first authorship.
[2] Lead contact

https://doi.org/10.1016/j.bioactmat.2024.08.016
Received 5 May 2024; Received in revised form 30 July 2024; Accepted 17 August 2024

ROS and pro-inflammatory cytokines, finally creating a positive feedback loop that delays the DW healing [6–11]. In clinical settings, the treatments of DW primarily include glycemic control, debridement, administration of antibiotics, and repetitive dressing changes [12]. However, these treatments did not simultaneously target chronic inflammation and inferior vascularization of DW [10-12]]. Additionally, debridement of DW is invasive and painful, while repetitive dressing changes and frequent administration of antibiotics are awkward, which may induce life-threatening infections caused by multidrug-resistant bacteria in the wound site [13,14]. To successfully heal DW and improve patient outcomes, it is crucial to develop a painless and convenient therapy capable of simultaneously managing chronic inflammation and vascularization.

During the past few decades, topical wound dressing combined with advanced drug delivery systems has been developed for simultaneous modulating macrophage polarization and angiogenesis at the DW site [8,15–17]. These topical wound dressings include nano/micro carriers, tissue engineering scaffolds, and hydrogels, which indeed avoid tedious dressing changes and overuse of antibiotics and successfully deliver anti-inflammatory and pro-angiogenic drugs into wounds [8,15–17]. However, along with wound healing, the gradually formed wound clots or scar tissues will become physical barriers that hinder drug molecules from penetrating the deep wound bed, thus decreasing their efficacy [18,19]. In recent years, microneedles (MN), as a minimally invasive and transdermal drug delivery system consisting of an array of microscale needles, has attracted widespread attention in dermatological treatment [18,20,21]. To date, various types of MN, such as solid, drug-coated, hollow, hydrogel, or dissolvable MN, have been successfully developed for DW treatment [21,22]. However, solid, drug-coated, or hollow MN needs troublesome drop-off after punching micropores or finishing drug delivery into skin wound [21,22]. Conversely, the dissolvable MN can be completely absorbed in the skin without worrying about MN removal and bio-hazardous wastes [22,23]. In addition, along with MN biodegradation, the dissolvable MN could transdermally release the encapsulated drugs for a long term, finally continuously functioning on the wound bed [22,23]. Thus, this study intends to develop a novel dissolvable MN-based wound dressing for DW treatment.

To realize that, the base material selected for fabricating this dissolvable MN is deemed to be critical. Acellular dermal matrix (ADM), a highly biomimetic dermal material acquired by the removal of cellular components in normal dermal tissues (NDT), is mainly composed of collagens, elastin, growth factors, cytokines, and adhesive proteins, and showed low immunogenicity, high biocompatibility, and good biodegradability [24–26]. These advantages render ADM to be a promising dermal matrix-mimetic material for fabricating dissolvable MN. However, the ADM is unchangeable in physiochemical morphology, and cannot be processed into the shape of microscale needles. Enlighted by published literature [27,28], blocky ADM was digested into a gel state and then modified with photo-crosslinking material to synthesize a methacrylated ADM-based hydrogel (ADMMA-GEL) through the amide bond reaction between methacryloyl groups and amino functional groups under ultraviolet excitation. Due to its physiochemical tailorability and shape fidelity, this ADMMA-GEL was selected as the base material for preparing our dissolvable MN (ADMMA-MN).

To endow this ADMMA-MN showing superior anti-inflammatory and pro-angiogenic capacities, specific drugs or bioactive substances should be encapsulated. In the past few decades, the discovery of exosomes made a revolutionary contribution to cell biology [29]. Exosomes, nano-sized particles released by most cells in the body, can serve as unique carriers of bioactive proteins, mRNAs, and miRNAs, and participate in cell-cell communication [29]. Moreover, many studies determined that exosomes exhibited superior biocompatibility, low immunogenicity, and therapeutic targetability [30,31]. These merits made the exosomes a potential bioactive substance encapsulating into ADMMA-MN. Recent studies showed that platelet-derived exosomes (PLT-Exos) have great efficacy in tissue regeneration owing to procoagulant activity and hemostasis, angiogenesis, immunomodulation, and regulation of cellular behaviors [32–35]. More importantly, compared with other cell sources and fluids used for exosome isolation, large amounts of platelets can be easily obtained using minimally invasive procedures for abundant PLT-Exos isolation [35]. Thus, PLT-Exos was selected as the bioactive substance for endowing our ADMMA-MN with anti-inflammatory and pro-angiogenic capacities.

Based on the above considerations, a dissolvable MN-based wound dressing (PLT-Exos@ADMMA-MN) was fabricated for transdermal and long-term delivery of anti-inflammatory and pro-angiogenic PLT-Exos to accelerate DW healing (Fig. 1). Firstly, an ADMMA-GEL with photo-crosslinking ability and physiochemical tailorability was synthesized as the base material for preparing our wound dressing. In-vitro studies found that this ADMMA-GEL showed fast-gelling performance, suitable biodegradability, excellent biocompatibility, and pro-angiogenic capacities. Then, PLT-Exos was selected as the encapsulating substance due to its favorable safety, easy accessibility, anti-inflammatory, and pro-angiogenic functions. After determining the minimum effective concentration of PLT-Exos encapsulation, PLT-Exos was mixed with ADMMA-GEL to fabricate PLT-Exos@ADMMA-MN. Lastly, in-vivo studies were performed to determine that PLT-Exos@ADMMA-MN could continuously and transdermally deliver PLT-Exos into the DW site to switch macrophage phenotype and stimulate angiogenesis, thus promoting DW healing.

2. Results and discussion

2.1. Preparation and characterization of rat-derived ADM

ADM is mainly made up of collagen and elastin, and this collagen-rich network of ADM provides a platform for mucosal epithelialization and neovascularization [36,37]. According to the origin source of dermal tissue, it can be classified into allogenic ADM or xenogeneic ADM [36,37]. More recently, fish skin-derived ADM has attracted special attention, because of fewer animal ethical restrictions, low risk of infection transmission, and lower cost of donor tissue acquisition [38]. Although various studies stated that both allogenic ADM and xenogeneic ADM show low antigenicity and are suitable for DW healing, several comparative studies indicated that the xenogeneic ADM presents a higher risk of inducing short-lived acute inflammation than the allogenic ADM [39,40]. Considering that the difficulty of DW healing is largely caused by chronic inflammatory response [6,41], the materials selected for preparing our MN should have low immunogenicity and superior biocompatibility. In this study, a streptozotocin-induced diabetic rat was selected for the in-vivo experiment. For the aim of low immunogenicity and good biocompatibility, rat dermal tissues were harvested to prepare allogeneic ADM for our MN fabrication. In the clinical setting, our MN should be fabricated using human-derived ADM.

Ideal decellularization protocol should be capable of completely removing cellular components while preserving the original architectural, compositional, biochemical, and mechanical properties of the native extracellular matrix (ECM) [42,43]. To date, researchers have successfully developed various decellularization protocols for NDT with physical, chemical, and/or enzymatic treatments, but there is no methodological gold standard for NDT decellularization. To minimize the adverse effect of decellularization on native ECM and maximize the removal of cellular components, these methods are generally chosen for a combined application, owing that one of these treatments alone is insufficient [42,43]. Recently, M.L. Pérez developed a fast protocol for decellularizing human dermal tissues while maintaining the desired biomechanical and structural properties of NDT [44], in which sodium dodecyl sulfate (SDS) was applied to wash away cellular substances of human dermal tissues. Considering that ionic detergents, such as SDS, sodium deoxycholate (SDC), and so on, showed harmful impacts on the structures and components of native ECM [42,43], our study modified

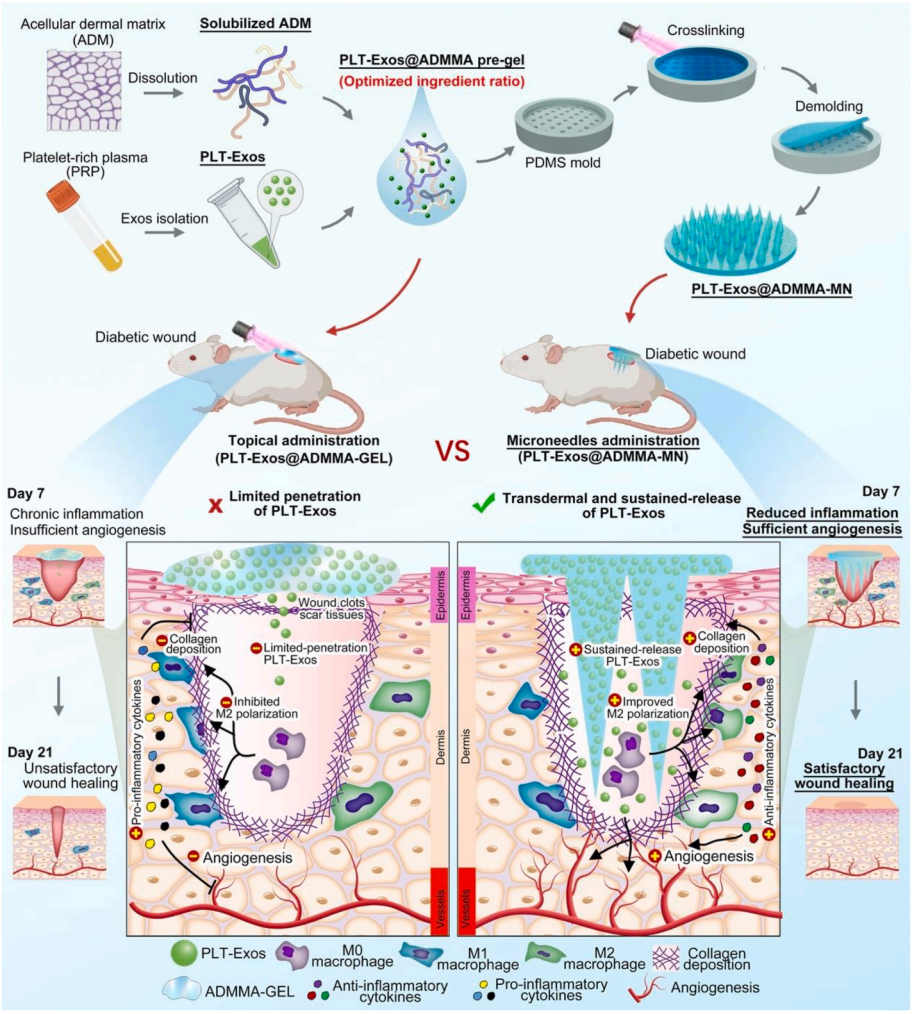

Fig. 1. Schematic illustration showing our dissolvable MN-based wound dressing (PLT-Exos@ADMMA-MN) preparation, merits, and mechanisms in DW treatment. In this study, PLT-Exos was mixed with biodegradable ADMMA-GEL to fabricate PLT-Exos@ADMMA-MN. Compared with the topical administration of PLT-Exos@ADMMA-GEL, this PLT-Exos@ADMMA-MN could transdermally deliver PLT-Exos into the dermis layer for a long time, thus switching more macrophages into M2 phenotype while stimulating neovascularization at the DW site for accelerating skin regeneration.

M.L. Pérez's decellularization protocol, replacing the 0.5 % SDS solution washing with 50 mM Tris-hydrochloride buffer containing 1 % Triton X-100 and 1.5 M KCl. The procedures of our decellularization protocol are shown in Fig. 2A.

As shown in Fig. 2B, the residual deoxyribose nucleic acid (DNA) in our ADM was nearly undetectable, which satisfies the minimum standard of decellularized scaffolds (50 ng/mg) [44]. Besides, there was no obvious 4′,6-diamidino-2-phenyl-indole (DAPI)-positive nuclear substances observed in our ADM (Fig. 2C). In addition, hematoxylin & eosin (H&E) and masson's trichrome (MT)-stained images showed that the histological structure of ADM was similar to NDT, including the microvascular structure and collagen arrangement (Fig. 2C). Using a scanning electron microscope (SEM), our ADM revealed a similar and unbroken microstructure to NDT (Fig. 2C). Considering that collagen I and elastin are major constituents of NDT, immunofluorescent images showed that collagen I and elastin were well reserved in our ADM (Fig. 2C). These results indicated that our decellularization protocol is capable of rapidly removing cellular components from rat dermal tissue without jeopardizing its natural structures and components.

2.2. Preparation and characterization of photo-crosslinkable methacrylate ADM hydrogel

In view that our ADM presented a blocky appearance with unchangeable physical morphology, it cannot be processed into the shape of microscale needles. Herein, to change the physiochemical tailorability of our ADM, it was firstly solubilized and then chemically reacted with methacrylic anhydride (MA) to form amide bonds, thus generating a methacrylate ADM (ADMMA) (Fig. 2D). To reveal the successful methacrylation on ADM, Fourier transform infrared (FTIR) spectra of ADM or ADMMA were recorded in the range of 4000-400 cm^{-1} (Fig. S1). Compared to the ADM, the hydroxyl peak or amino peak of ADMMA around 3300 cm^{-1} was decreased and widened, which may result from the formation of hydrogen bonds between MA and the amino groups in the ADM. Specifically, the peaks at 1334 cm^{-1} and 1341 cm^{-1} mainly attributed to the C–N stretching vibration, and the peaks at 1341 cm^{-1} were shifted to the location of 1334 cm^{-1} when the ADM was transformed to the ADMMA, indicating the potential methacrylation on ADM.

With the help of a photo-initiator (Irgacure 2959) [45], four ADMMA pre-gels with different concentrations of ADMMA powders (3 %, 4 %, 5 %, 6 %) (w/v) were prepared, which can change into a gel state under ultraviolet and achieve the sol-gel transition process. Using a dynamic rotational rheometer, the viscoelastic properties of the four ADMMA pre-gels were measured, including the mechanical strength and gelling time. A frequency-sweep test was applied for the assessment of storage modulus (G′) of the four ADMMA pre-gels (3 %, 4 %, 5 %, 6 %) (w/v), and the result showed 5%ADMMA-GEL exhibited the highest modulus

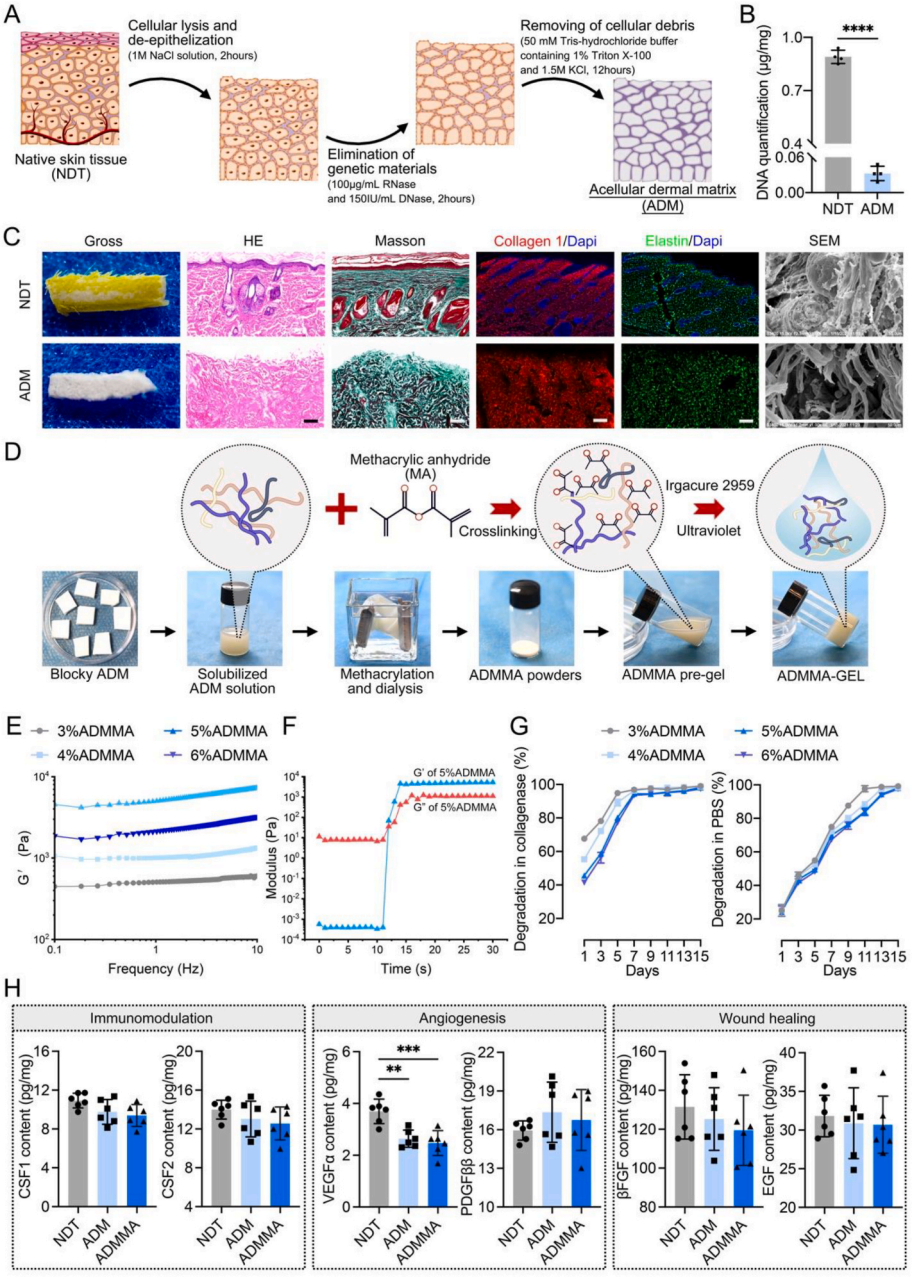

Fig. 2. (A) Schematic illustration showing the procedures of acellular dermal matrix (ADM) fabrication; (B) DNA residues in the NDT or ADM; (C) Gross images, H&E, MT, Collagen1/DAPI, Elastin/DAPI staining, and SEM were used to evaluate the morphological changes of the dermal matrix before and after decellularization, and DAPI staining was used to observe DNA residues, Scale bar = 100 μm; (D) The procedures of fabricating ADMMA powders, ADMMA pre-gel, and ADMMA-GEL; (E) Frequency-sweep assessment of storage modulus of ADMMA pre-gel with different concentration; (F) Storage modulus (G′) and loss modulus (G″) of 5%ADMMA-GEL; (G) Degradation rate of ADMMA-GEL with different concentration in collagenase or PBS environment; (H) The content of cytokines involved in immunomodulation, angiogenesis, and wound healing within the NDT, ADM, and ADMMA. Data are presented as mean ± SD (n = 4). **p < 0.0021, ***p < 0.0002.

(approximately 4550 Pa) (Fig. 2E). The irradiation of ultraviolet on the 5%ADMMA pre-gel for 12s made the storage modulus G′ superior to loss modulus G″, resulting in the hydrogel formation, demonstrating the property of fast gelling of the ADMMA-GEL (Fig. 2F). In addition, with the concentration increasing of ADMMA, the four kinds of ADMMA-GELs showed a gradually delayed degradation in both phosphate-buffered saline (PBS) and collagenase environments. Under the collagenase environment, 5%ADMMA-GEL was completely degraded for about 7 days (Fig. 2G). Under the PBS environment, the degradable rate of ADMMA-GEL was markedly decreased, and the time for 5%ADMMA-GEL complete degradation was extended to 15 days (Fig. 2G). In-vitro degradability evaluation predicted that the MN prepared with the ADMMA-GEL could be degraded absolutely in vivo, more suitable for clinical application compared to those MN fabricated with polymer materials [18].

Apart from collagen I and elastin, growth factors are the key components rendering biological activities to the ADM [46]. As the decellularization protocol of our study was modified for the aim of minimizing the adverse effect of acellular procedures on native ECM, growth factors and cytokines embedded within NDT should be well preserved. In this study, the NDT, ADM, or ADMMA were used to quantify the contents of growth factors and cytokines involved in immunomodulation (CSF1, CSF2), angiogenesis (VEGFα, PDGFββ), and wound healing (βFGF, EGF). As shown in Fig. 2H, the majority of

investigated growth factors and cytokines in the ADM or the ADMMA showed decreases more or less when compared with the NDT, while no significant differences were found between the ADM and the ADMMA. In particular, VEGFα in the ADM and the ADMMA decreased significantly when compared with the NDT. The processes of decellularization and physiochemical modification inevitably lead to the loss and inactivation of growth factors [42,43], more investigations involving decellularization optimization of NDT and physiochemical modification of ADM should be performed to improve this dilemma in the future.

2.3. Preparation and characterization of isolated PLT-Exos

Due to low immunogenicity, high stability, and easy storage, exosomes have been isolated or engineered as an effective and novel cell-free strategy for tissue repair or regeneration [29,47–49]. In the DW site, exosomes are important components regulating the diabetic microenvironment, and accumulating evidence confirmed that exosomes can promote wound closure and skin regeneration through various pathways, such as promoting angiogenesis, collagen fiber deposition, and inhibiting inflammation [50–52]. To date, exosomes isolated from diabetic wound-related fibroblasts (DWAF), adipose stem cells (ASCs), mesenchymal stem cells (MSCs), immune cells, platelets, amniotic epithelial cells (AECs), epidermal stem cells (ESCs), has been determined in promoting DW healing [49,51,52]. Among the cell types used for exosome isolation, only the platelets can be easily and abundantly obtained using minimally invasive procedures, and avoid the complicated and tedious cell culture to obtain sufficient supernatant for exosome isolation [35]. These advantages ensured the convenient application of PLT-Exos in clinical settings. In addition, previous studies have determined that PLT-Exos showed the function in hemostasis, vascularization, immunomodulation, and tissue repair [32–35]. Thus, we selected PLT-Exos as encapsulating substances to endow our MN with anti-inflammatory and pro-angiogenic capabilities.

In this study, the procedures of PLT-Exos isolation are shown in

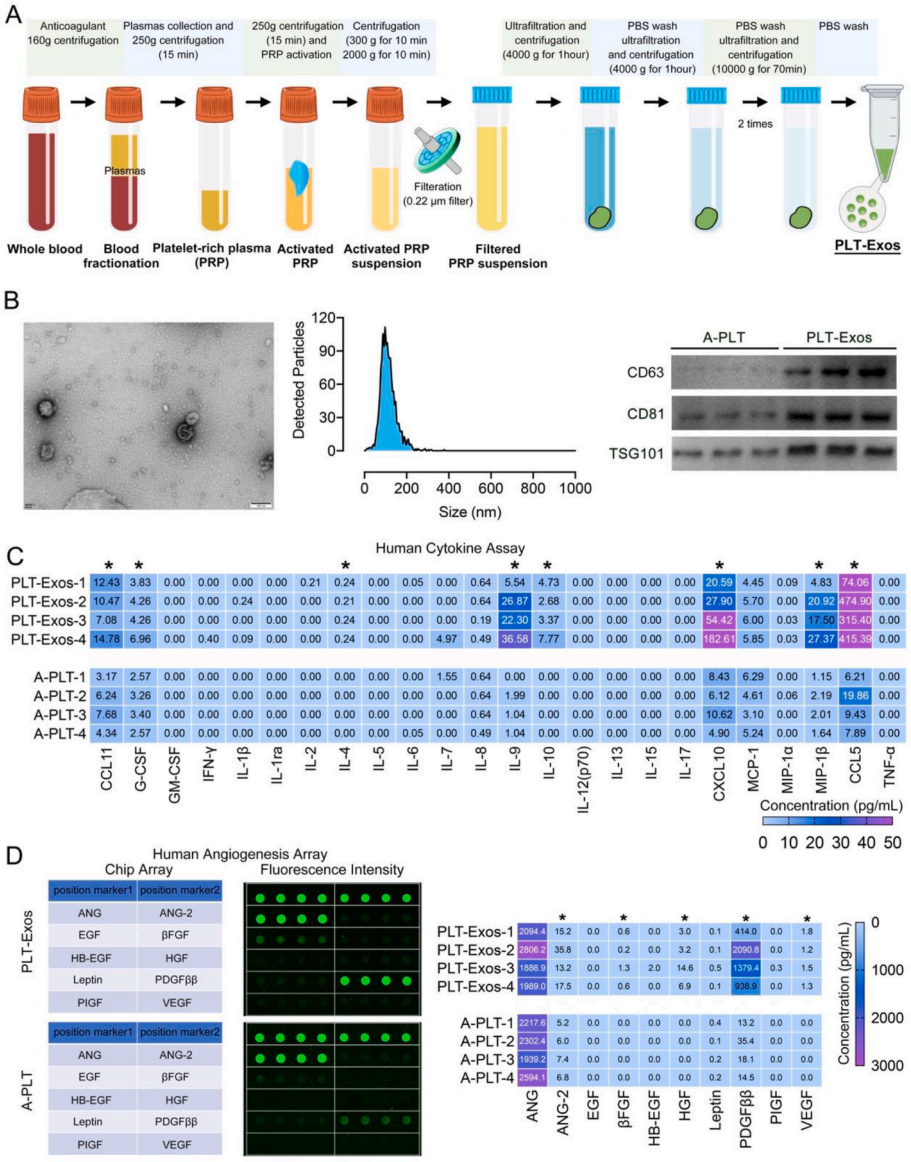

Fig. 3. (A) Schematic illustration showing the procedures of PLT-Exos preparation; (B) Typical TEM image of a PLT-Exo, NTA showing the size distribution of PLT-Exos, Western blot analysis of the exosome markers in the PLT-Exos, Scale bar = 100 nm; (C) Heat map showing the content of inflammatory cytokines in the PLT-Exos, the activated platelets (A-PLT) were also analyzed as a control; (D) Human angiogenesis array analysis of the samples of PLT-Exos or A-PLT, fluorescence signals of the ten angiogenic cytokines in PLT-Exos or A-PLT, heat map showing the content of angiogenic cytokines in PLT-Exos or A-PLT; "*" indicates significant difference between PLT-Exos and A-PLT.

Fig. 3A. After isolating PLT-Exos, transmission electron microscopy (TEM), nano visual tracking analysis (NTA), and western blotting for exosome markers were used together to fully identify these isolated exosomes. As shown in Fig. 3B, TEM and NTA show that the diameter of these isolated exosomes ranged from 40 nm to 100 nm, which is consistent with the previous literature [29]. Western blotting showed that these isolated exosomes were positive for specific exosomal surface markers (CD63, CD81, and TSG101), further confirming their identity. More importantly, the cargoes in these isolated exosomes were analyzed using Bio-Plex Pro Human Cytokine 27-plex Assay and Human Angiogenesis Array. After the platelets were activated, the main bioactive molecules in the platelets were released absolutely, thus these activated platelets (A-PLT) were selected as control. The Human Cytokine 27-plex Assay (Fig. 3C) showed that PLT-Exos contained anti-inflammatory cytokines (IL4, IL10, G-CSF) and chemotactic factors (CCL5, CCL11, CXCL10), while the Human Angiogenesis Array (Fig. 3D) showed that PLT-Exos are full of cytokines involved in angiogenesis (ANG-2, VEGF, PDGFββ) and wound healing (βFGF, EGF).

2.4. Determining the minimum effective concentration of PLT-Exos encapsulation

In consideration that the PLT-Exos have positive effects on promoting vascularization and inhibiting inflammatory response [32–35], PLT-Exos have been encapsulated into various materials for tissue repair, such as GelMA-based hydrogel with 10×10^{10} exosomes/mL for DW healing [53], thermosensitive hydrogel with 2 μg exosomes/μL for delaying osteoarthritis [54], PBS solution with 40 μg exosomes/mL for attenuating intervertebral disc degeneration [55]. More recently, a first-in-human clinical trial showed that allogeneic PLT-Exos (300 μg exosomes in 1 mL 0.9 % saline) injected subcutaneously adjacent to skin wound was a potential therapy for its healing [56]. According to those reports, it can be seen that the concentration of PLT-Exos encapsulated in the hydrogel remains controversial, and the minimum effective concentration of PLT-Exos mixing into our ADMMA-GEL needs further investigation. In this study, the minimum effective concentration of PLT-Exos encapsulating into ADMMA-GEL was determined by co-culturing human umbilical vein endothelial cells (HUVECs) with the four PLT-Exos@ADMMA-GELs (Fig. 4A), which were prepared with four gradient concentrations of PLT-Exos (0, 100, 200, 400 μg/mL),

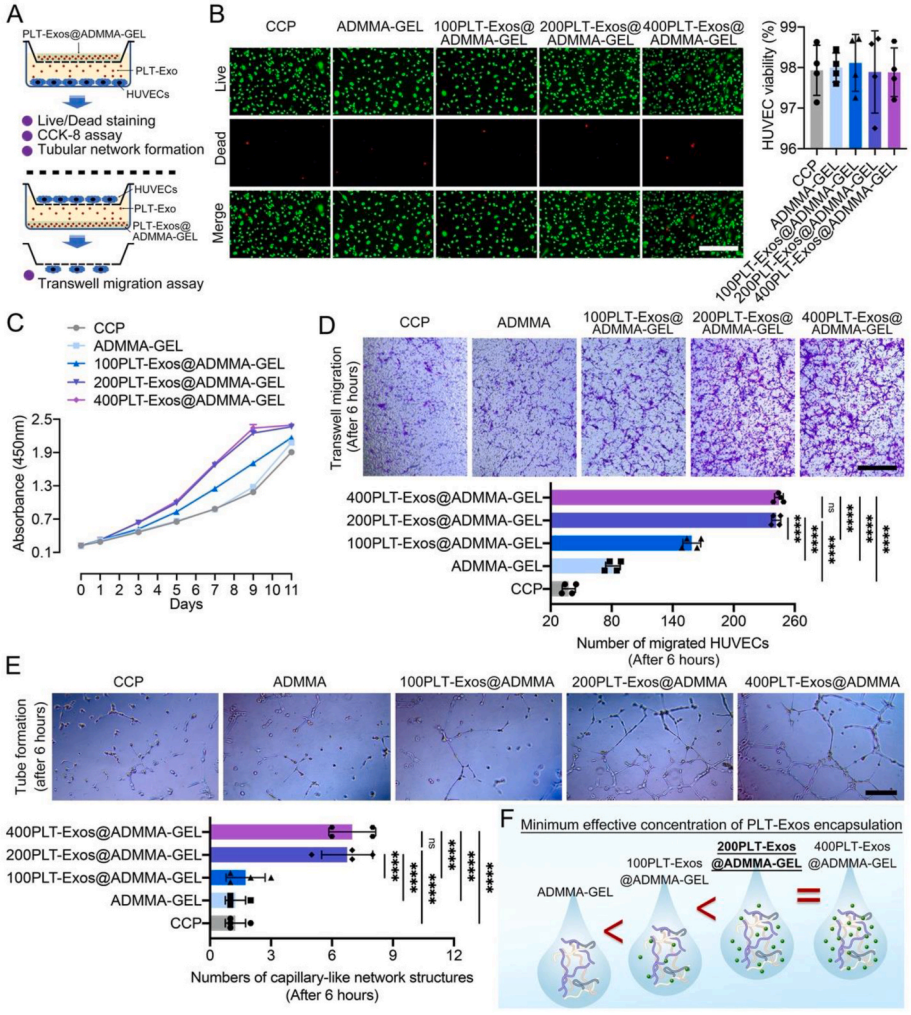

Fig. 4. (A) Schematic illustration showing the co-culturing system of HUVECs and PLT-Exos@ADMMA-GEL as well as evaluation experiments used for determining the minimum effective concentration of PLT-Exos encapsulation; (B) Cell viability of the four PLT-Exos@ADMMA-GELs using live/dead staining, fluorescent images show live (green) and dead (red) HUVECs cultured with the GELs, and the rate of live cells to total cells was calculated as cell viability, Scale bar = 100 μm; (C) CCK-8 assay was used to assess the HUVECs proliferation on the four GELs; (D) Transwell assay was used to assess the HUVECs migration under the influence of the four GELs, Scale bar = 100 μm; (E) The effect of different PLT-Exos@ADMMA-GELs on tube formation of HUVECs at 6 h. Scale bar = 100 μm; (F) Schematic illustration showing the minimum effective concentration of PLT-Exos encapsulation. Data are presented as mean ± SD (n = 4). *p < 0.0332, **p < 0.0021, ***p < 0.0002, ****p < 0.0001, and "ns" indicates no significance.

referenced in the human clinical trial [56].

To evaluate the cytocompatibility of the four PLT-Exos@ADMMA-GEL, Live/Dead staining analysis was performed after 24 h of culture. The Live/Dead staining results showed that the cell viability of the four PLT-Exos@ ADMMA-GELs was greater than 95 % and similar to the cell culture plate (CCP) without significant differences (Fig. 4B), indicating no cytotoxicity of these PLT-Exos@ADMMA-GELs. The low cytotoxicity provides a safety guarantee for its clinical translation. Additionally, the cell counting kit-8 (CCK-8) assay showed that the HUVECs proliferation enhanced along with the increasing encapsulation of PLT-Exos. Meanwhile, the HUVECs cultured on the 200PLT-Exos@ADMMA-GEL (containing 200 μg/mL PLT-Exos) or the 400PLT-Exos@ADMMA-GEL (containing 200 μg/mL PLT-Exos) presented a similar proliferation curve, proliferating significantly better than the HUVECs on the other hydrogels or CCP (Fig. 4C). As for in-vitro angiogenesis activity of these PLT-Exos@ADMMA-GELs, our results showed that the 200PLT-Exos@ADMMA-GEL or the 400PLT-Exos@ADMMA-GEL exhibit a significantly greater number of migrated HUVECs than the other hydrogels or CCP, and no significant difference was found between the 200PLT-Exos@ADMMA-GEL and the 400PLT-Exos@ADMMA-GEL (Fig. 4D). Moreover, the tube formation assay showed that the HUVECs under the stimulation of the 200PLT-Exos@ADMMA-GEL and the 400PLT-Exos@ADMMA-GEL formed more capillary-like network structures rather than the branching structures with discontinuous tubular walls observed in other hydrogels or CCP. Quantitatively, the 200PLT-Exos@ADMMA-GEL and the 400PLT-Exos@ADMMA-GEL have a significantly greater number of tubules than the other hydrogels or CCP due to the stimulation of higher levels of PLT-Exos (Fig. 4E). This result showed that the PLT-Exos has a saturated concentration of encapsulation in our ADMMA-GEL, indicating 200 μg/mL is the minimum effective concentration of PLT-Exos encapsulating into ADMMA-GEL (Fig. 4F).

2.5. Fabrication and characterization of PLT-Exos@ADMMA-MN

As presented in Fig. 5A, PLT-Exos@ADMMA-MN was fabricated by a micro-molding approach using a self-designed PDMS mold [18,22]. The parameters of our PDMS mold are detailed in Fig. S2. Briefly, after lyophilized PLT-Exos dissolved in the ADMMA pre-gel with 200 μg/mL concentration, this hybrid solution was filled into a mold and cross-linked under ultraviolet. Subsequently, after drying and de-molding, the patch of PLT-Exos@ADMMA-MN was prepared and stored for the following experiment. This patch shows a diameter of 22 mm, in which 688 microneedles are distributed equidistantly at intervals of 600 μm (Fig. 5B). Under SEM, each PLT-Exos@ADMMA-MN appeared tapered in

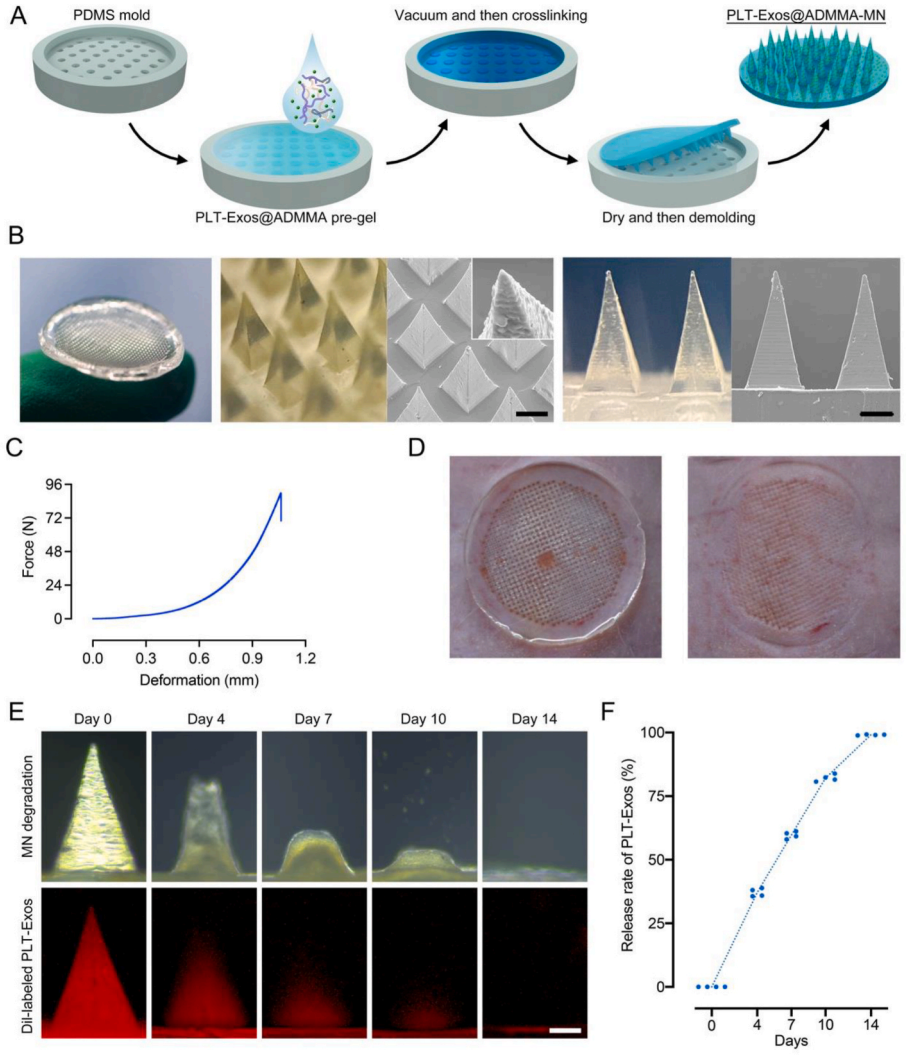

Fig. 5. (A) Schematic illustration showing the procedures of PLT-Exos@ADMMA-MN preparation; (B) Morphological images and SEM images of PLT-Exos@ADMMA-MN, Scale bar = 200 μm; (C) Mechanical properties characterization of the PLT-Exos@ADMMA-MN; (D) Photograph of the pores left after PLT-Exos@ADMMA-MN was applied to the rat skin; (E) Representative images of the micrographs of MN and the Dil-labeled PLT-Exos distribution of MN after immersed in 37 °C PBS for 0, 4, 7, 10, and 14 days; (F) Quantitative analysis of Dil-labeled PLT-Exos release in-vitro at day 0, 4, 7, 10, and 14; Data are presented as mean ± SD (n = 4).

shape, with a height of about 800 μm and a bottom margin of about 350 μm (Fig. 5B).

As shown in Fig. 5C, the maximum failure force of the entire microneedle array (688 needles) was about 90 N, which was significantly greater than the minimum force required to pierce skin (0.1 N) [57]. Furthermore, the back skin of an SD rat was used to test the effect of the PLT-Exos@ADMMA-MN puncture. The MN was applied to the rat skin for 2 min and then removed. In Fig. 5D, well-arranged microporous channels in the rat skin can be observed, indicating that our MN was strong and sharp enough to penetrate the skin.

DW healing is a long-time repair process owing to persistent inflammation and poor vascularization at the wound site [6–9]. Therefore, our MN with the ability for slow-sustained release of anti-inflammatory and pro-angiogenic PLT-Exos is helpful and necessary. To detect the PLT-Exos distribution in our MN and the release profile of PLT-Exos from our MN, the PLT-Exos were labeled by a red fluorescence dye (Dil) before being encapsulated into the ADMMA pre-gel, and confocal laser scanning microscopy (CLSM) was used to

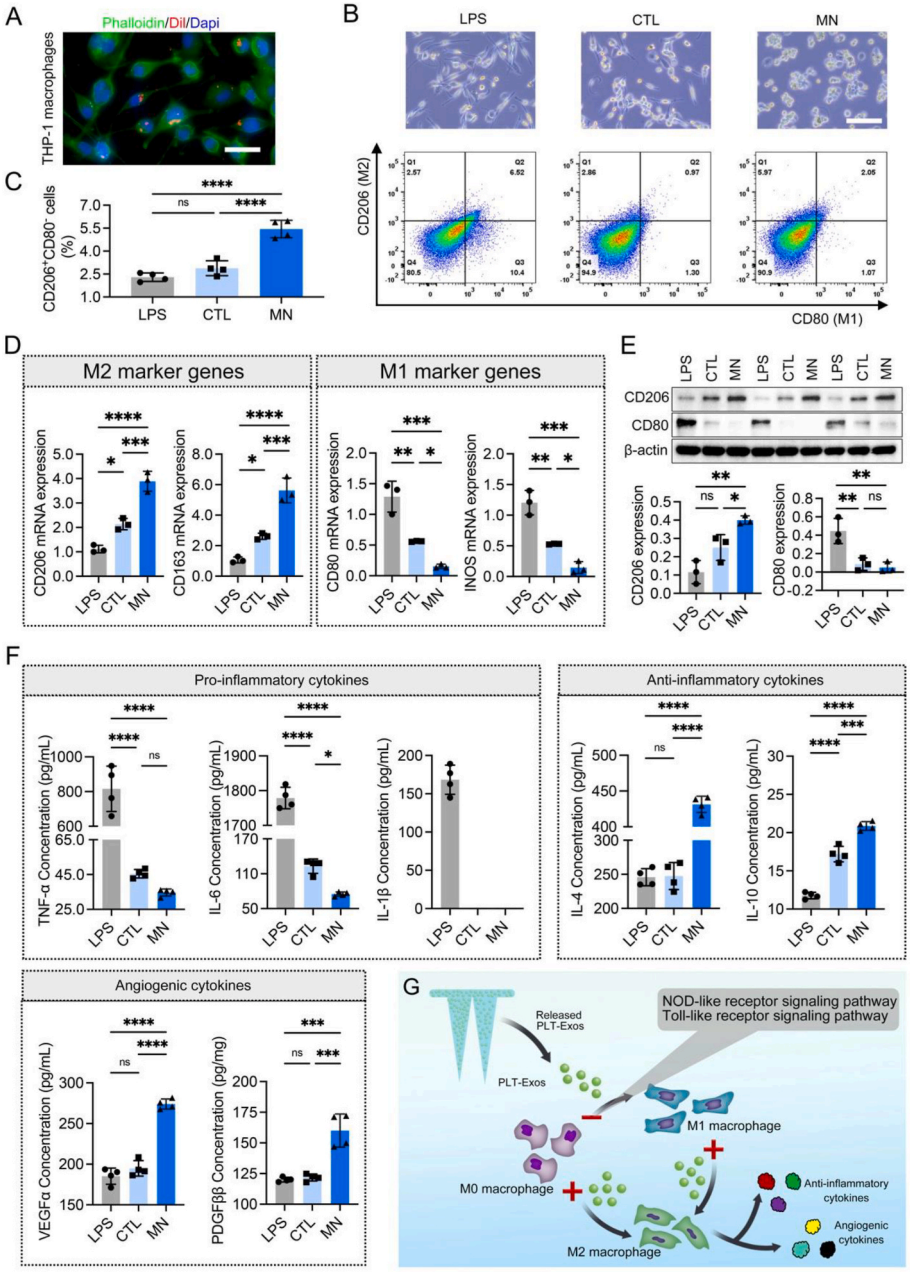

Fig. 6. In-vitro anti-inflammatory capacity of the PLT-Exos@ADMMA-MN. (A) CLSM imaging showing the uptake PLT-Exos released from PLT-Exos@ADMMA-MN by THP-1 macrophages, Scale bar = 10 μm; (B) Microscope images and flow cytometry plots of THP-1 macrophages in the LPS, CTL, or MN group, Scale bar = 100 μm; (C) Quantitative data indicating the ratio of $CD206^{+}CD80^{-}$positive cells (M2 macrophages) in the LPS, CTL, or MN group, n = 4; (D) Expression levels of M1 (INOS and CD80) and M2 (CD163 and CD206) phenotypic markers in THP-1 macrophages from the LPS, CTL, or MN group, n = 3; (E) Western-blot images and semi-quantitative data showing the expression of CD206 and CD80 in THP-1 macrophages from the LPS, CTL, or MN group, n = 3; (F) The contents of pro-inflammatory cytokines (TNF-α, IL-6 and IL-1β), anti-inflammatory cytokines (IL-10 and IL-4), and angiogenic cytokines (VEGFα and PDGFββ) in the supernatants of THP-1 macrophages from the LPS, CTL, or MN group, n = 4; (G) Schematic illustration showing the mechanisms of PLT-Exos@ADMMA-MN on switching macrophage polarization, secreting inflammatory and angiogenic cytokines. Data are presented as mean ± SD. *p < 0.0332, **p < 0.0021, ***p < 0.0002, ****p < 0.0001, and "ns" indicates no significance.

observe the distributions of red fluorescence (Dil-labeled PLT-Exos) within our MN. The Dil-labeled PLT-Exos@ADMMA-MN were immersed in PBS at 37 °C, and red fluorescence was recorded by CLSM at different time points. The gradual decrease in the fluorescence area of MN tips was indicative of PLT-Exos release with increasing immersion time (Fig. 5E). Along with our MN degradation, the MN released about 37.12 % of Dil-labeled PLT-Exos on day 4, 59.71 % of Dil-labeled PLT-Exos on day 7, and 82.08 % of Dil-labeled PLT-Exos on day 10 in PBS, while the red fluorescence area of MN tips disappeared almost on day 14 (Fig. 5F). These findings imply that our PLT-Exos@ADMMA-MN has sustainable PLT-Exos release properties in vitro.

2.6. In-vitro anti-inflammatory capacity of PLT-Exos@ADMMA-MN

Macrophages, as innate immune cells, play important roles in host defense, wound healing, and immune regulation [58]. Macrophages show high plasticity that can be polarized to classically activated macrophages (M1), involved in pro-inflammatory responses; alternatively, activated macrophages (M2), optimizing local inflammation suitable for tissue repair and remodeling [58]. In the DW site, excessive pro-inflammatory M1 macrophages and deficient anti-inflammatory M2 macrophages result in chronic inflammation, delaying wound healing [59,60]. Thus, therapies capable of reversing this abnormal macrophage polarization could be applied to accelerate DW healing. PLT-Exos is a natural nanoparticle obtained from blood platelets, known for its anti-inflammatory effects [32,35,54]. As determined in our array results, PLT-Exos cargo several kinds of anti-inflammatory cytokines (Fig. 3C). We predicted that our PLT-Exos@ADMMA-MN could regulate macrophage phenotypes and inflammatory cytokines secretion to orchestrate the DW microenvironment. Herein, the efficacy of our MN on macrophage polarization and inflammatory cytokines secretion was investigated by culturing THP-1 macrophages with the PLT-Exos@ADMMA-MN.

Firstly, to determine that the released PLT-Exos from our MN can be internalized by THP-1 macrophages, PLT-Exos were labeled by a red fluorescence dye (Dil) before preparing PLT-Exos@ADMMA-MN. As shown in Fig. 6A, Dil-labeled PLT-Exos could be dispersedly distributed around the nuclei of macrophages, suggesting the successful uptake of PLT-Exos by THP-1 cells. Additionally, flow cytometry was performed to quantitatively analyze macrophage polarization under stimulations of PLT-Exos@ADMMA-MN. CD206 and CD80 were used as markers of M2 and M1 macrophages, respectively, for flow cytometry staining. THP-1 macrophages treated with a culture medium containing lipopolysaccharide (LPS) were set as positive control (named as LPS group), while those THP-1 macrophages cultured with the medium without any supplements were set as negative control (named as CTL group). The culture medium containing PLT-Exos@ADMMA-MN was named as MN group. As shown in Fig. 6B, macrophages co-cultured with the PLT-Exos@ADMMA-MN displayed a small round morphology that resembled to M2 phenotype, while M1 macrophages were flat with multiple pseudopodia. Flow cytometry analysis indicated that the ratio of $CD206^{+}CD80^{-}$positive cells (M2 macrophages) was only 2.29 ± 0.28 % and 2.88 ± 0.49 % in the LPS group or CTL group but sharply increased to 5.44 ± 0.57 % in the MN group (Fig. 6B and C).

To further confirm the polarization status of macrophages, CD206 and CD163 genes (M2 marker) and CD80 and INOS genes (M1 marker) were measured by quantitative reverse transcription polymerase chain reaction (qRT-PCR). Compared to the LPS group, the macrophages in the MN group expressed significantly higher CD206 and CD163 genes, as well as lower CD80 and INOS genes (Fig. 6D). Meanwhile, using Western blot, the MN group showed significantly higher expression of CD206 compared to the LPS and CTL groups (Fig. 6E). In addition, the pro-inflammatory cytokines (TNF-α and IL-6) secreted by THP-1 macrophages in the CTL and MN groups were similar without significant differences, but significantly lower than that of the LPS group. In particular, IL-1β secreted by THP-1 macrophages in the CTL or MN group were undetectable (Fig. 6F). As for the anti-inflammatory cytokines (IL-10 and IL-4), the supernatants from the LPS or CTL group contain significantly lower levels of IL-10 and IL-4 than the MN group (Fig. 6F). Additionally, the THP-1 macrophages in the MN group secret more VEGFα and PDGFββ into cell supernatants in comparison with the THP-1 macrophages of the CTL or LPS groups (Fig. 6F). Those results indicated that the macrophages under the stimulation of PLT-Exos@ADMMA-MN tend to polarize into the M2 phenotype rather than the M1 phenotype, and secret more anti-inflammatory and pro-angiogenic cytokines (Fig. 6G).

To further identify the mechanisms of PLT-Exos@ADMMA-MN switching macrophage polarization, RNA sequencing (RNA-Seq) was used to assess changes in messenger RNA (mRNA) levels in THP-1 macrophages after culturing with the CCP (CTL group) or PLT-Exos@ADMMA-MN (MN group) (Fig. 7A). A total of 28475 genes were identified, and the analysis of differentially expressed genes (DEGs) showed that the expression of 2882 genes was up-regulated and 1932 genes were down-regulated in the THP-1 macrophages of the MN group compared to that of the CTL group (Fig. 7B). Using the gene expression profiles (GEPs) of our RNA-Seq, cell-type identification by estimating relative subsets of RNA transcripts (CIBERSORT) analyzed the subsets of the THP-1 macrophages in the CTL or MN group according to literature [61], and the result showed more THP-1 macrophages polarization into M2 phenotype (Fig. 7C), which was accordance to the result of flow cytometry analysis (Fig. 6B and C). Gene ontology (GO) analysis was implemented to analyze the function of the DEGs. As shown in Fig. S3, 149 DEGs were associated with biological processes of “positive regulation of cytokine production”, and the MN caused the downregulation of genes involved in “positive regulation of cytokine production”. KEGG pathway analysis of the DEGs associated with “positive regulation of cytokine production” revealed the potential mechanisms of inflammatory cytokines release, such as NOD-like receptor signaling pathway (including 17 genes), Toll-like receptor signaling pathway (including 11 genes) (Fig. 7D). The “NOD-like receptor signaling pathway” has been known to mediate the immune response to cellular injury and stress [62]. As shown in Fig. 7E, the MN group caused a negative regulation of the “NOD-like receptor signaling pathway”, including the signal transducer and activator of transcription (STAT1) and interferon regulatory factor (IRF3/7). STAT 1 is a very important transcription factor, which can convert anti-inflammatory macrophages into a pro-inflammatory phenotype via STAT/IRF3/7 pathway, and secret pro-inflammatory cytokines [63]. In addition, the MN group inhibited the activation of “Toll-like receptor signaling pathway” (Fig. 7F), including Toll-like receptor 8 (TLR8) and interferon regulatory factor (IRF3/7), which is involved in preventing macrophage polarization toward the M2 phenotype [64,65]. Thus, these results of RNA-seq suggest that our MN decreased THP-1 macrophages polarization into M1 phenotype, and then inhibited the secretion of pro-inflammatory cytokines by inhibiting the “NOD-like receptor signaling pathway” and “Toll-like receptor signaling pathway” (Fig. 6F).

2.7. In-vitro pro-angiogenic capacity of PLT-Exos@ADMMA-MN

Adequate angiogenesis plays an important role in DW healing, as neovascularization could deliver oxygen and nutrients to the wound site and transport away ROS and pro-inflammatory cytokines [66,67]. Our array results showed that PLT-Exos contains various angiogenic factors (Fig. 3D), and previous studies indicated that PLT-Exos facilitates angiogenesis [32,34,35], thus it was selected as a supplemental component for preparing our MN. For evaluating its pro-angiogenic ability, CCK-8 assay, cell scratch test together with transwell migration assay, and tube formation assay were performed to observe the proliferation, migration, and tube formation of HUVECs under the influence of our MN. In our study, HUVECs cultured within a medium containing VEGFα (6 ng/mL) were set as positive control (named as VEGF group) [17], while the HUVECs cultured with the medium without

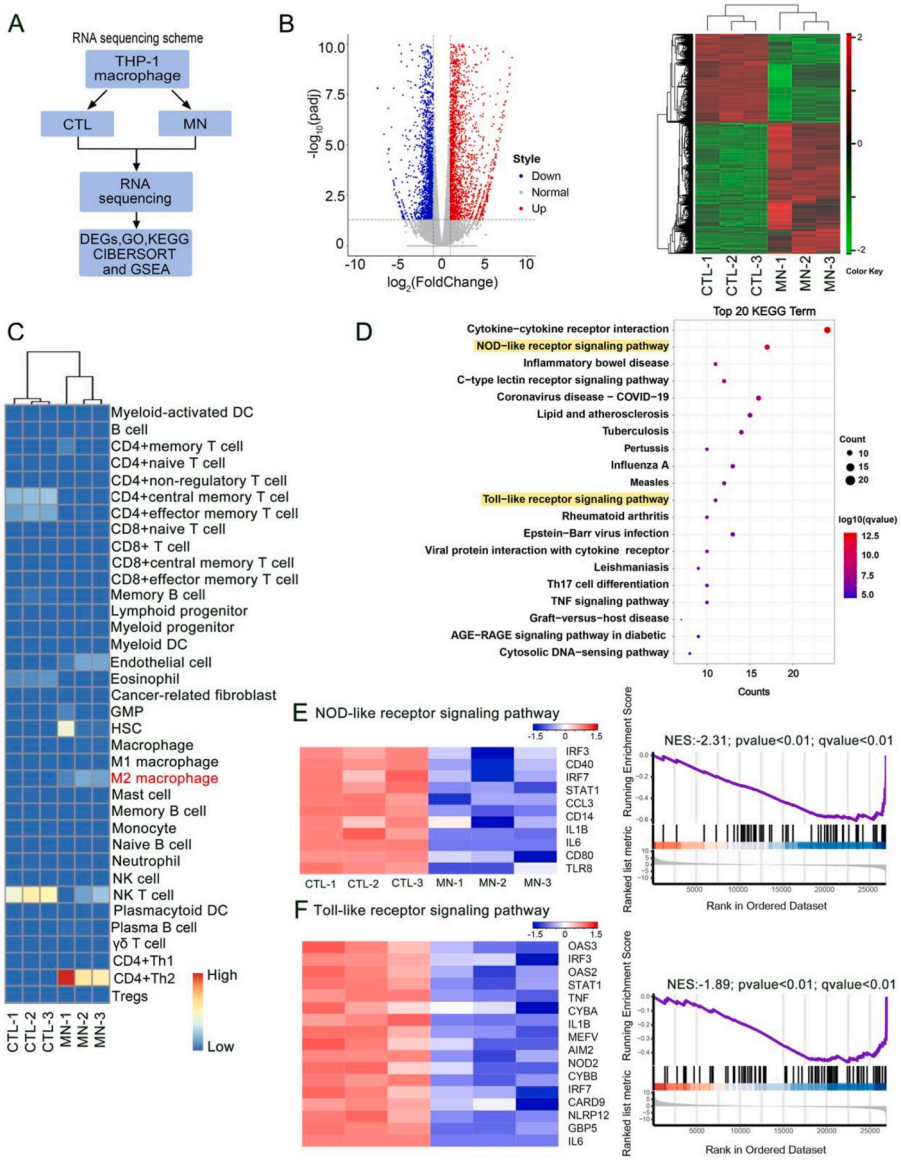

Fig. 7. RNA sequencing for elucidating the mechanisms of PLT-Exos@ADMMA-MN switching macrophage polarization. (A) RNA sequencing scheme for the THP-1 macrophages in the CTL or MN group; (B) The DEGs in the MN group compared with the CTL group. Heatmap analysis reveals the DEGs that all up-regulated or down-regulated in the MN group and CTL group; (C) CIBERSORT analysis of gene sets for the subsets of the THP-1 macrophages in the CTL or MN group; (D) The top 20 up-enrichment of KEGG pathways in the MN group compared with CTL group; (E) Heatmap representation and GSEA analysis of gene sets for NOD-like receptor signaling pathway; (F) Heatmap representation and GSEA analysis of gene sets for Toll-like receptor signaling pathway; NES, normalized enrichment score.

any supplements were set as negative control (named as CTL group). The HUVECs co-cultured with PLT-Exos@ADMMA-MN were named the MN group.

As shown in Fig. 8A, several Dil-labeled PLT-Exos dispersedly distributed around the nuclei of HUVECs, indicating the successful uptake of PLT-Exos by HUVECs. The CCK-8 assay showed that the MN group and the VEGF group significantly increased the proliferation of HUVECs on days 3 and 7 in comparison with the CTL, but the HUVECs in the MN group were slightly slower in proliferation than the VEGF group without significant difference (Fig. 8B). The cell scratch test together with the transwell migration assay revealed that our MN was similar to VEGFα in stimulating the HUVEC migration (Fig. 8C and D). The tube formation assay found that the MN group or the VEGF group shows significantly more capillary-like tubes than the CTL group, while the capillary-like tubes in the MN group formed significantly less than that of the VEGF group (Fig. 8D). Overall, our results indicated that PLT-Exos released from PLT-Exos@ADMMA-MN contributed greatly to angiogenesis in-vitro.

PI3K/Akt/HIF-1α pathway was closely related to angiogenesis during DW healing [68]. To determine if the PI3K/Akt/HIF-1α pathway was involved in the process of PLT-Exos to stimulate angiogenesis, Western blot analysis was performed to measure the expression level of p-PI3K, PI3K, p-AKT, AKT, HIF-1α, and GAPDH in HUVECs. The results revealed that the HUVECs in the MN group could enhance the expression of p-PI3K, p-AKT, and HIF-1α, similar to the HUVECs in the VEGF group (Fig. 8E). These findings suggested that PLT-Exos@ADMMA-MN stimulated the PI3K/Akt/HIF-1α pathway, which in turn increased the angiogenic activities of HUVECs in-vitro (Fig. 8F).

2.8. *PLT-Exos@ADMMA-MN capable of transdermal and sustained delivery of PLT-Exos in-vivo*

To evaluate our MN on transdermal delivery of PLT-Exos, the distribution of Dil-labeled PLT-Exos in the dermis layer was observed by a

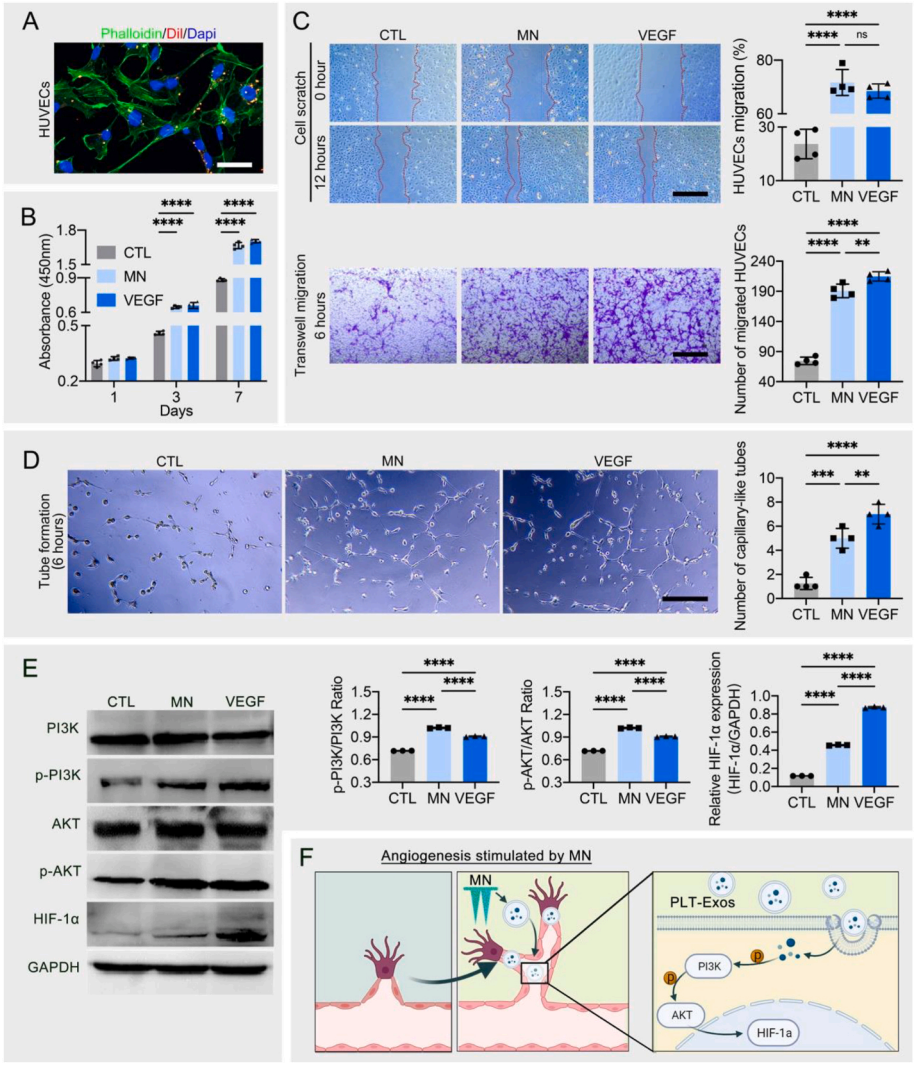

Fig. 8. In-vitro angiogenic capacity of the PLT-Exos@ADMMA-MN. (A) CLSM imaging showing the uptake PLT-Exos released from PLT-Exos@ADMMA-MN by HUVECs, Scale bar = 10 μm; (B) On days 1, 3, and 7, the CCK-8 assay was used to assess the HUVECs proliferation under the influence of PLT-Exos@ADMMA-MN, n = 4; (C) Cell scratch test together with transwell migration assay was used to assess the HUVECs migration under the influence of the PLT-Exos@ADMMA-MN, n = 4, Scale bar = 100 μm; (D) The effect of PLT-Exos@ADMMA-MN on tube formation of HUVECs at 6 h, n = 4, Scale bar = 100 μm; (E) Western blot analysis of the expression levels of PI3K, P-PI3K, AKT, P-AKT, and HIF-1***α*** of HUVECs under the influence of the PLT-Exos@ADMMA-MN, n = 3; (F) Schematic illustration showing that PLT-Exos@ADMMA-MN increased the angiogenic activities of HUVECs in-vitro via stimulating PI3K/Akt/HIF-1α pathway; Data are presented as mean ± SD, *p < 0.0332, **p < 0.0021, ***p < 0.0002, ****p < 0.0001, and "ns" indicates no significance.

CLSM at 30 min and 7 days following topical (TO) administration or microneedles (MN) administration of Dil-labeled PLT-Exos@ADMMA-GEL (named TO or MN group) (Fig. 9A). At 30 min post-treatment, both TO and MN groups showed red fluorescence in the dermis tissue, indicating the presence of PLT-Exos. Particularly, strong fluorescent areas were shown at the wedge-shaped openings in the MN group, where PLT-Exos@ADMMA-MN was penetrated in the wounds. This strong fluorescence indicated that more encapsulated PLT-Exos were accumulated at the microneedle penetration site (Fig. 9B). At 7 days post-treatment, owing to the physical barrier of wound clots or scar tissues, the wounds in the TO group showed no red fluorescence in the dermis tissue, while the MN group showed obvious red fluorescence in the dermis tissue (Fig. 9B). These results imply that our MN could transdermally deliver PLT-Exos to the dermis layer.

To evaluate the capability of our MN on sustained delivery of PLT-Exos, the distribution of Dil-labeled PLT-Exos in the DW was observed using the in vivo imaging system (IVIS) from day 0 to day 14 following intradermal (ID) injection or microneedles (MN) administration of Dil-labeled PLT-Exos (named ID or MN group) (Fig. 9A). As shown in Fig. 9C, the rats in the MN group presented a strong Dil-positive red fluorescence signal at the penetration site, which remained visible for at least 14 days, while the rats in the ID group lost nearly all of the signals by day 7, implying the PLT-Exos@ADMMA-MN capable of sustained release of PLT-Exos at least 14 days in-vivo.

Overall, the transdermal and sustained delivery of PLT-Exos enabled by PLT-Exos@ADMMA-MN can attract more attention in the medical or cosmetic field owing to its user-friendly convenience.

2.9. *PLT-Exos@ADMMA-MN accelerated diabetic wound healing in-vivo*

In-vitro experiments have demonstrated the promising anti-inflammatory and proangiogenic potential of PLT-Exos@ADMMA-MN. We investigated the wound healing efficiency of PLT-Exos@ADMMA-MN in vivo using a streptozotocin-induced diabetic rat wound model. The schematic diagram of our in-vivo study is presented in Fig. 10A, in which the rats with DW were treated by intradermal injection of PLT-Exos solution (ID, the same PLT-Exos in our MN), topical administration of PLT-Exos@ADMMA-GEL (TO, the same PLT-Exos in our MN), or

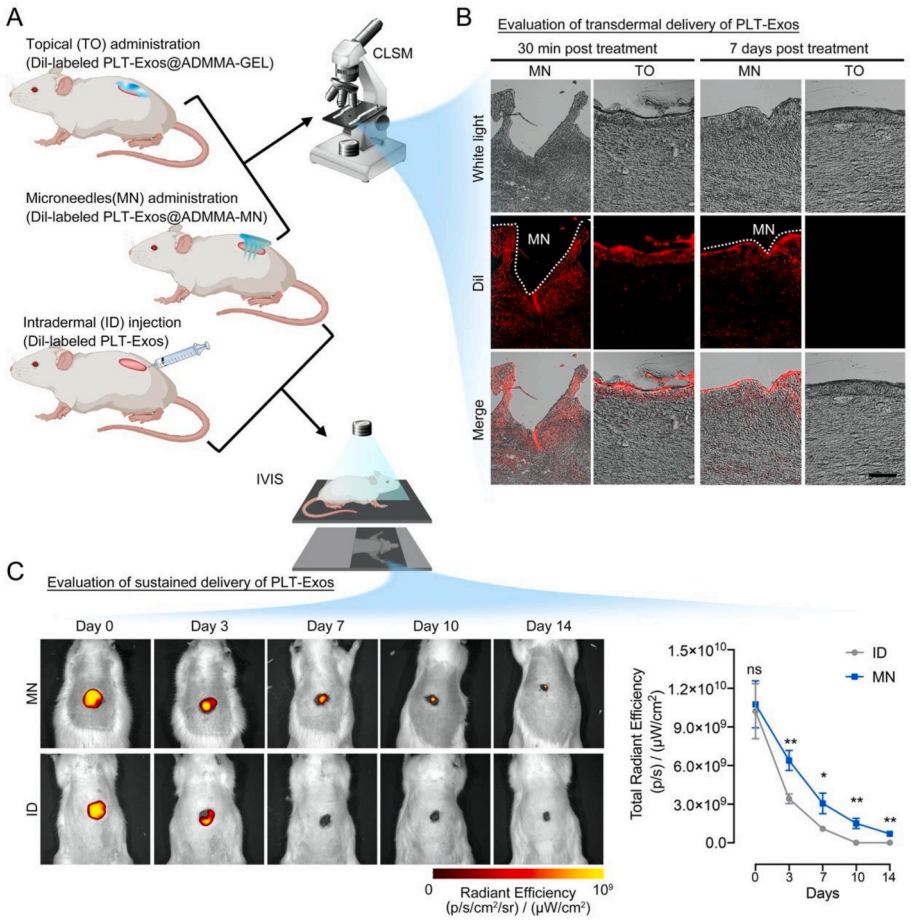

Fig. 9. (A) Schematic illustration showing in-vivo experiment design for evaluating the capability of PLT-Exos@ADMMA-MN on transdermal and sustained delivery of PLT-Exos; (B) CLSM images of Dil-labeled PLT-Exos distribution in the DW sections after topical administration of Dil-labeled PLT-Exos@ADMMA-GEL (TO) or microneedles administration of Dil-labeled PLT-Exos@ADMMA-MN (MN), Scale bar = 100 μm; (C) IVIS images showing the Dil-labeled PLT-Exos distribution in the DW site after intradermal injection of Dil-labeled PLT-Exos (ID) or microneedles administration of Dil-labeled PLT-Exos@ADMMA-MN (MN); Data are presented as mean ± SD (n = 4). *p < 0.0332, **p < 0.0021, and "ns" indicates no significance.

microneedles administration of PLT-Exos@ADMMA-MN (MN).

As shown in Fig. 10B, representative images of DW after various treatments at different treatment times are presented. In comparison to the ID group, the TO group only slightly decreased the wound area at different treatment times. Compared with the ID or TO group, the MN group showed a faster rate of wound healing starting on day 7, and the DW in the MN group showed a significant decrease on days 7, 14, and 21 ($P < 0.05$) (Fig. 10C). The histological structures of diabetic wounds after different treatments were evaluated by H&E and MT staining on day 21. As shown in Fig. 10D–H&E-stained images revealed that large residual scars and immature skins (IS) were depicted in the ID or TO group, while most of the healed skins in the MN group presented mature skins (MS). Re-epithelialization and wound contraction are the main approaches to skin wound healing [69], the re-epithelialization rate (%) was measured for quantitative assessment of wound healing. The re-epithelialization rate of the MN group was the highest among the three groups, and the difference was statistically significant ($P < 0.05$) (Fig. 10E). The collagen expression in the skin was investigated by MT staining. The results showed a larger area of collagen fibers in the MN group than in the other groups. According to the area rate of MT staining-positive collagen, the collagen deposition in the MN group was significantly more obvious than in the ID or TO group ($P < 0.05$) (Fig. 10E).

There are two advantages of our MN. Firstly, our MN has an array of tips with a length of 800 μm, which coincides with the depth of the dermis layer. This feature makes them suitable for accurate intradermal delivery of PLT-Exos. By contrast, these PLT-Exos delivered by topical administration would be obstructed on the wound surface owing to the gradually formed physical barrier (wound clots or scar tissues), thus only functioning at the early stage of wound healing. Secondly, our MN can serve as a sustained delivery system for PLT-Exos, which continuously suppresses inflammation and improves angiogenesis through their cargos (anti-inflammatory and angiogenic cytokines) (Fig. 3C and D). Thirdly, the ADMMA used in our MN was derived from NDT, and shows high biomimetics and superior degradability. The ADMMA, as the penetrated MN degradation, will provide biomimetic materials and support for dermis formation.

2.10. PLT-Exos@ADMMA-MN inhibited inflammation in vivo

Generally, DW healing undergoes four continuous and overlapping phases: hemostasis, inflammation, proliferation, and remodeling [10,70,71]. At the inflammation stage, macrophages infiltrated into the wound site are polarized towards the M1 phenotype with phagocytic and clearance properties, followed by a transition from the M1 phenotype to the M2 phenotype, which secreting anti-inflammatory and angiogenic cytokines to provide a favorable microenvironment for successful wound healing [6,60,71]. Remarkable advances in research have shown that macrophage-predominated immunomodulation is one of the key mechanisms of DW healing, directly influencing its healing speed and quality [6,59,60,71,72]. Thus, the efficacy of our MN on the M1-to-M2 polarization and the expression of inflammatory cytokines were

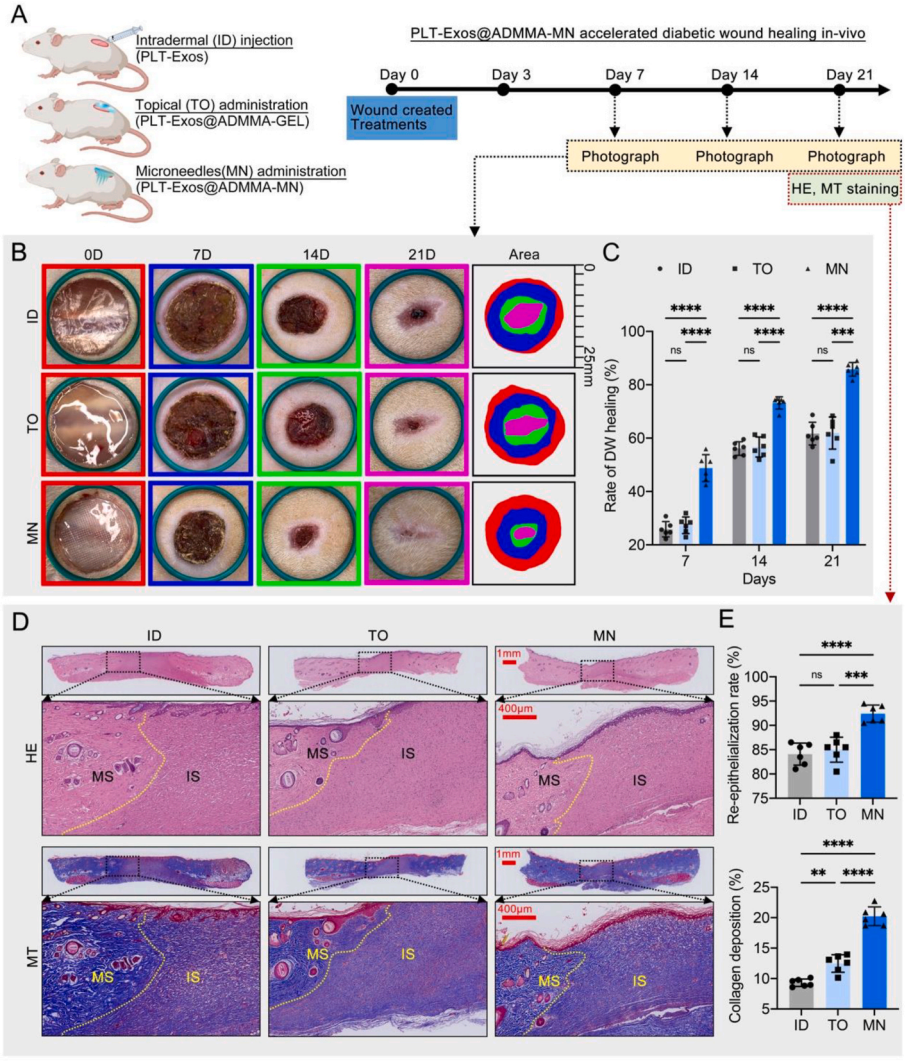

Fig. 10. In-vivo performance of the PLT-Exos@ADMMA-MN on DW healing. (A) Schematic illustration showing the design and evaluation of PLT-Exos@ADMMA-MN for the treatment of DW; (B) Gross images of DW healing after the treatment of ID, TO, MN at day 0, 7, 14 and 21, Diameter of the green band = 25 mm; (C) Closure rates of DW among the three group; (D) H&E and MT staining for the dorsal skin of diabetic rat after different treatments, immature skins (IS), mature skins (MS), scale bar = 1 mm or 400 μm; (E) Statistical analysis of re-epithelialization and collagen deposition at the DW site after different treatments; Data are presented as mean ± SD (n = 6). *p < 0.0332, **p < 0.0021, ***p < 0.0002, ****p < 0.0001, and "ns" indicates no significance.

evaluated at this early stage.

On days 3 and 7, immunostaining of wound sections was conducted to label M1 and M2 macrophages with anti-86 or anti-CD206 antibodies, respectively (Fig. 11A). Immunofluorescent images showed heavily infiltrated CD206-positive cells within the wounds of the MN group compared with the wounds of the ID and TO groups, verifying increased quantities of anti-inflammatory M2 macrophages (Fig. 11B). Quantitatively, the M2/M1 ratio in the MN group was significantly higher than those in the ID and TO groups, indicating that our MN activated a smooth M1-to-M2 transition of macrophages in the early stage of wound healing (Fig. 11C). As for the expression of inflammatory cytokines, the MN group showed significantly lower levels of TNF-α and IL-6, as well as higher levels of IL-10 and IL-4 than other groups (Fig. 11D). These results indicated that our MN can optimize the inflammatory response at the early stage of wound healing.

This optimized immune environment in the MN group can be explained through the following two mechanisms: 1) the ADM used for preparing MN was allogeneic with low immunogenicity and good biocompatibility, which contains growth factors regulating the maturation and differentiation of immune cells (CSF1, CSF2). The CSF1 were beneficial for macrophage survival, proliferation, and phenotypic switch [73]; 2) our MN encapsulated lots of PLT-Exos, which cargo several kinds of anti-inflammatory cytokines (Fig. 3C). Those cytokines could regulate macrophage phenotypes and inflammatory cytokines secretion to orchestrate the DW microenvironment.

2.11. PLT-Exos@ADMMA-MN promoted angiogenesis in vivo

Following the inflammation stage, the blood vessels will gradually invade the wounds in the proliferation stage to eliminate metabolic waste, transmit oxygen and nutrients for tissue regeneration, and release paracrine signals regulating special cells associated with skin regeneration [74]. Thus, the MN with angiogenesis stimulation in this proliferation stage is a critical property for wound healing. To evaluate the vascularization potential of our MM, microcomputed tomography (micro-CT) combined with the injection of radiopaque contrast agents was performed at days 7 and 14 post-treatment to visualize angiogenesis in the wounds. In addition, immunofluorescent staining of CD31 and αSMA was also used to observe angiogenesis of the wound site. As shown in Fig. 12A, the micro-CT images displayed that the MN group formed more blood vessels and capillary tributaries within the wounds compared with the ID and TO groups. Quantitatively, the vessel volume

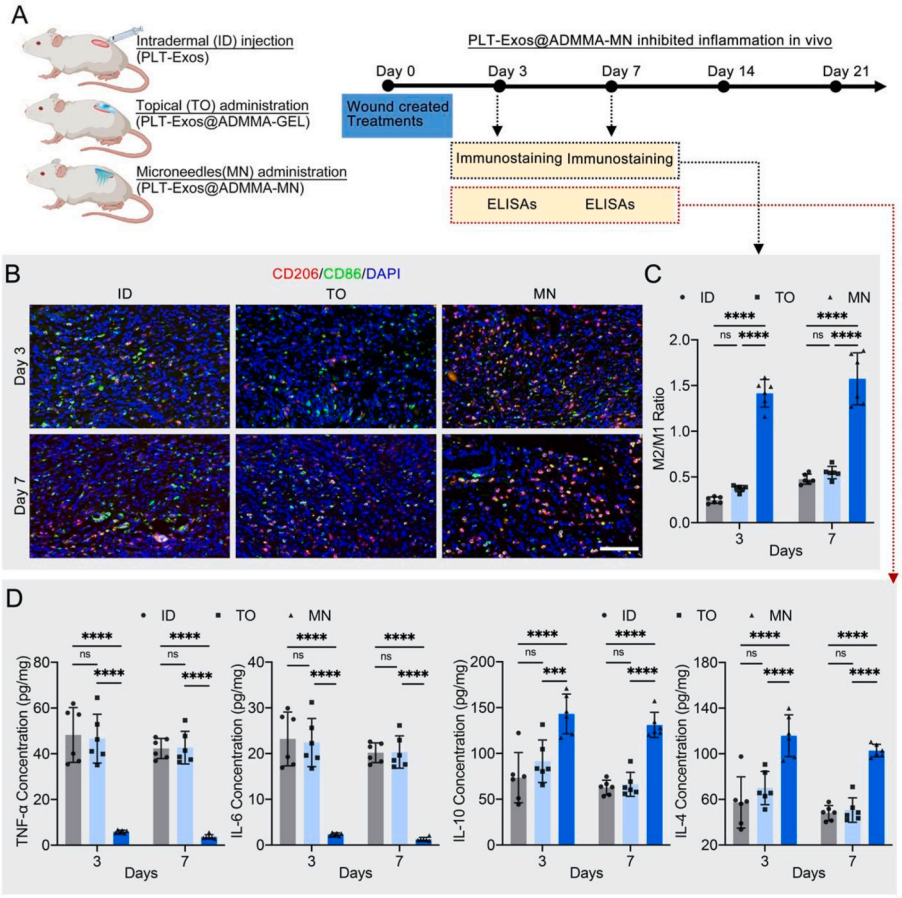

Fig. 11. In-vivo performance of the PLT-Exos@ADMMA-MN on inhibiting inflammation. (A) Schematic illustration showing the design and evaluation of PLT-Exos@ADMMA-MN on inhibiting inflammation; (B) Immunofluorescent staining of skin sections of wound area for CD86 (M1 marker) and CD206 (M2 marker) at days 3 and 7 after injury, Scale bars = 100 μm; (C) Quantification of the M2/M1 ratio in immunofluorescent images from the DW site; (D) ELISA analysis of TNF-α, IL-6, IL-10, and IL-4 from the wound tissue lysates extracted at days 3 and 7 after injury; Data are presented as mean ± SD (n = 6). *p < 0.0332, **p < 0.0021, ***p < 0.0002, ****p < 0.0001, and "ns" indicates no significance.

(%) in the MN group was significantly higher than that of the ID and TO groups on days 7 and 14 (Fig. 12B). The mean vessel diameter of the MN group was significantly higher than that of the ID group on day 7, while the MN group showed a lower value for the mean vessel diameter than that of the ID and TO groups on day 14(Fig. 12C), which reflected that blood vessels gave off fine capillary tributaries, suggesting that the MN induced a high functional angiogenic response. Histologically, CD31 and αSMA, respectively revealing vascular endothelial cells and pericytes within skin wounds, can be used to observe capillaries and mature arteries [75]. The immunofluorescent staining of CD31 and αSMA showed that the MN group showed significantly more CD31-positive endothelial cells on day 7 in comparison with the ID and TO groups, reflecting a rapid endothelial cell response and robust capillary growth (Fig. 12D and E). On day 14, CD31 and αSMA-labeled vessels increased more obviously in the MN group when compared with the ID and TO groups (Fig. 12D and E), which can be attributed to part of the CD31-positive capillaries regressing into mature arteries, thus bringing nutrients, immune cells, and oxygen to healing wounds. These results indicated that our MN can stimulate vascular formation and maturation at the proliferation stage of wound healing.

Toward this enhanced neovascularization in the MN group, some putative mechanisms may be that: 1) the ADMMA contains serval kinds of angiogenic factors (Fig. 2H), which can promote vascular ingrowth by directly or indirectly modulating signaling pathways associated with angiogenesis; 2) Another important mechanism is the activation of signaling pathways in endothelial cells and vascular smooth muscle cells by angiogenic factors (Fig. 3C) in PLT-Exos, which stimulate endothelial cell migration and proliferation and induce undifferentiated cells to differentiate into vascular smooth muscle cells, thereby facilitating angiogenesis and maturation; 3) under the influence of the PLT-Exos, more pro-healing M2 macrophage accumulated within the DW site of MN group (Fig. 11B), which would release more angiogenic cytokines into DW site, such as PDGF and VEGF, to enhance vascularization.

3. Conclusion

In summary, to prepare a dissolvable MN-based wound dressing (PLT-Exos@ADMMA-MN), a novel ADMMA-GEL, showing photo-crosslinking, physiochemical tailorability, fast-gelling performance, suitable biodegradability, excellent biocompatibility, and pro-angiogenic capacities, was fabricated as the base material for MN preparation. PLT-Exos were encapsulated into this ADMMA-GEL to fabricate PLT-Exos@ADMMA-MN, due to its favorable safety, easy accessibility, and anti-inflammatory and pro-angiogenic functions. By applying to rat DW treatment, our results demonstrated that PLT-Exos@ADMMA-MN could transdermally and continuously deliver the encapsulated PLT-Exos into the DW site to switch M1-to-M2 macrophage transition and stimulate angiogenesis, thus promoting DW healing. Therefore, this PLT-Exos@ADMMA-MN is an excellent and convenient wound dressing, that can be used in DW treatment via simultaneous management of chronic inflammation and vascularization.

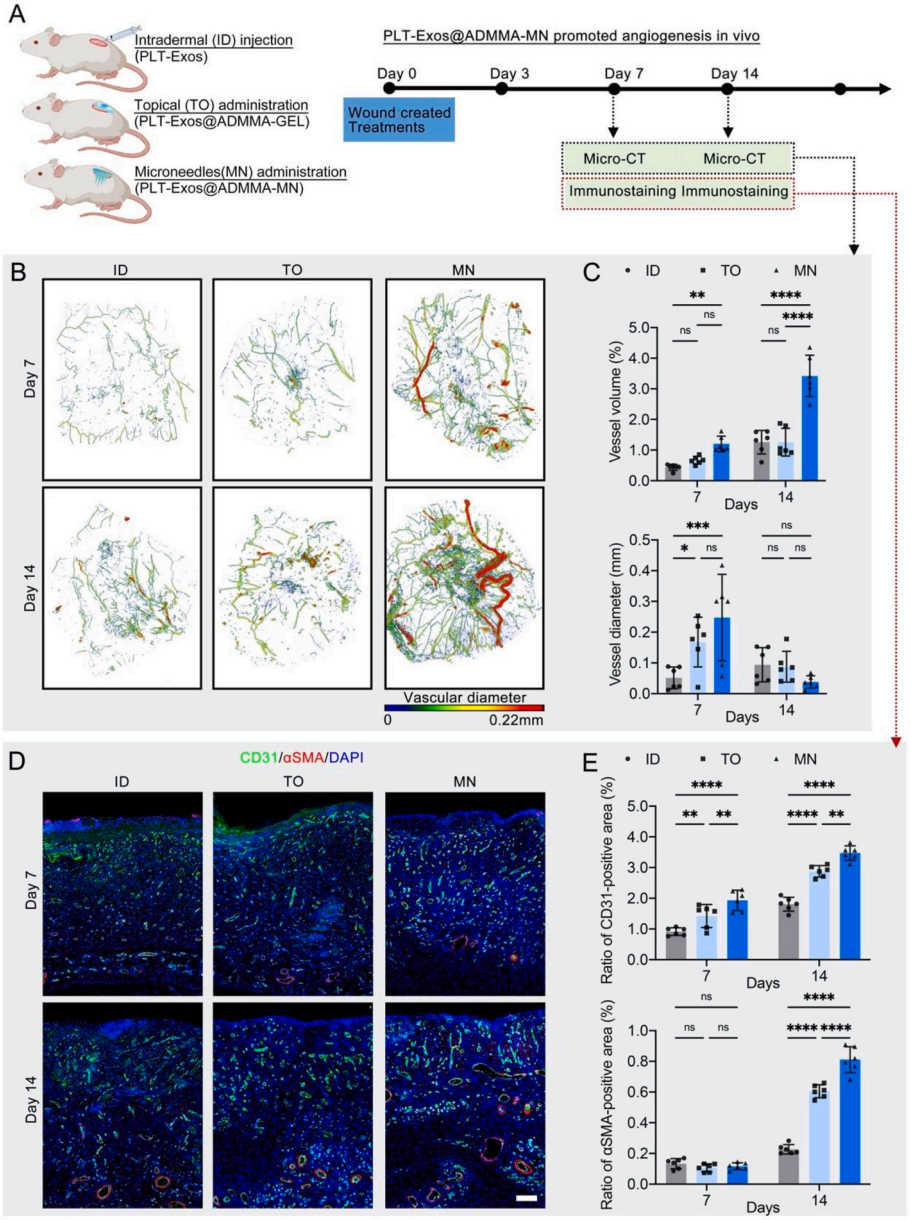

Fig. 12. In-vivo performance of the PLT-Exos@ADMMA-MN on promoting angiogenesis. (A) Schematic illustration showing the design and evaluation of PLT-Exos@ADMMA-MN on promoting angiogenesis; (B) Pseudocolored micro-CT image of the wound microvasculature correlated with vessel thickness at day 7 and day 14 after injury; (C) Quantitative analysis of vessel volume (%) and vascular diameter; (D) Immunofluorescent staining of skin sections of wound area for vascular formation and maturation using anti-CD31 and αSMA at days 7 and 14 after injury, Scale bars = 100 μm; (E) Quantification of CD31 or αSMA-positive area per field; Data are presented as mean ± SD (n = 6). *p < 0.0332, **p < 0.0021, ***p < 0.0002, ****p < 0.0001, and "ns" indicates no significance.

4. Materials and methods

Ethical approval

The Ethics Committee of Chenzhou No. 1 People's Hospital approved the experimental procedures for the use of male SD rats (3 months old) and the collection of human blood for PLT-Exos isolation (No. 2023001).

4.1. Preparation of rat-derived ADM

Native skin tissues were harvested from the dorsum of adult SD rats, and the hair and subcutaneous fascia were removed and washed with PBS solution containing 1 % penicillin-streptomycin-amphotericin B (Procell, CHN) for decontamination. After the skin was incubated in 1M NaCl solution for 2 h to induce cellular lysis by osmosis and facilitate the de-epithelization, they were digested with nuclease solution (100 μg/mL RNase and 150IU/mL DNase) (Sigma, USA) at 37 °C for 2 h for the elimination of genetic material. Then, 50 mM Tris-hydrochloride buffer containing 1 % Triton X-100 and 1.5M KCl (Aladdin, CHN) was used to wash out cellular debris for 12 h. Finally, PBS washing was performed to remove residual reagents. After that, the tissues were lyophilized to obtain ADM. During decellularization, 1 % penicillin-streptomycin-amphotericin B solution and protease inhibitor (1 tablet/100 mL, S8820-20TAB, Sigma) were added to the aforementioned solutions, while no protease inhibitor was added into nuclease solution.

4.2. Characterization of rat-derived ADM

DNeasy Blood&Tissue Kit (Qiagen, USA) together with PicoGreen DNA assay kit (Invitrogen, USA) was used to quantify the DNA content

in the NDT and ADM. After NDT and ADM were fixed and embedded in paraffin, they were sliced and stained with H&E, MT, anti-collagen I/DAPI, or elastin/DAPI (immunofluorescent staining). H&E combined with DAPI staining was used to assess the removal of cellular components in ADM. MT and immunofluorescent staining were used to evaluate the collagen and elastin in ADM. SEM (Mira3 LMH, Tescan, Czech Republic) was applied to observe the microstructure of ADM.

For immunofluorescent staining, sections were incubated with primary antibodies overnight at 4 °C. The primary antibodies applied here were as follows: rabbit anti-collagen I (1:200; Abcam, UK), and rabbit anti-elastin (1:200; Abcam, UK). After washed in PBS, sections were incubated in Alexa Fluor 488-conjugated secondary antibodies (Chemicon, USA), and then observed with a Fluorescent Microscope (ApoTome 2, Carl Zeiss, Germany). For SEM observation, NDT and ADM were fixed with glutaraldehyde overnight, dehydrated with a series of ethanol solutions, and then lyophilized. After the gold sputtering was treated, they were observed under SEM.

4.3. Preparation of ADMMA

The freeze-dried ADM was ground into powder and digested by 1 mg/mL pepsin in a 0.01 mol/L hydrochloric acid solution at 37 °C for 72 h with constant stirring. After removing undigested particles with 100 mesh wire screens, the ADM solution was adjusted to pH 8.0–9.0. Then, MA (Aladdin, CHN) was added to this ADM solution with a dropping rate of 0.5 mL/min, at a ratio of 1 mL MA per gram of freeze-dried ADM. After stirred at 37 °C for acylation reaction, this ADM solution was dialyzed in a dialysis bag for 72 h to remove the residual MA, and then lyophilized to acquire ADMMA powders.

4.4. Characterization of ADMMA-GEL

The desired concentration of ADMMA pre-gels (3 %, 4 %, 5 %, 6 %) (w/v) was made by dissolving ADMMA powders in sterile PBS along with 0.05 % (w/v) of photoinitiator (Irgacure 2959, Aladdin, CHN). To evaluate the rheological properties of the four ADMMA-GELs, the storage modulus (G′) and the loss modulus (G) were measured by a rotational rheometer (Anton Paar MCR 302e) with a plate geometry (25 mm dia, 3 mm gap). Firstly, a frequency sweep (0.1–10 Hz) was conducted on the four ADMMA pre-gels with 1 % strain after UV crosslinking at 25 °C. Additionally, a time sweep was also conducted on ADMMA-GELs for 30 s at 25 °C with a frequency of 10 Hz, 1 % strain. FTIR spectra were recorded in the range of 4000-400 cm^{-1} and at a resolution of 2 cm^{-1} by FTIR spectrophotometer (Nicolet 6700, Thermo Fisher Scientific Inc.). The spectra plots represented the average of 32 scans.

In-vitro biodegradation of these ADMMA-GELs was assessed using PBS solution or collagenase I solution (Sigma, USA). After measuring the original weight (W0) of the freeze-dried ADMMA-GEL, they were incubated in the PBS solution or collagenase I solution (1 mg/mL) for 1, 3, 5, 7, 9, 11, 13, and 15 days. After these incubated ADMMA-GELs were washed with deionized water and freeze-dried again, they were weighed at each time point (Wd). The degradation rate was calculated by the following equation: Degradation Rate (%) = [(W0−Wd)/W0] × 100 (%).

To evaluate the protein maintenance during fabricating ADMMA powders, the growth factors in the ADMMA powders involved in immunomodulation (CSF1, CSF2), angiogenesis (VEGFα, PDGFββ), and wound healing (βFGF, EGF) were evaluated using corresponding ELISA kits, which was listed in Table S1.

4.5. Preparation and identification of isolated PLT-Exos

After whole blood was taken from healthy donors, citrate dextrose solution A (ACD-A) was added as an anticoagulant. Then, 40 mL of whole blood was centrifuged at 160 g for 10 min to obtain platelet-containing plasma. After that, this platelet-containing plasma was centrifuged again at 250 g for 15 min. The supernatant plasma was discarded, and the platelet pellet was resuspended in the residual plasma to obtain 4 mL platelet-rich plasma (PRP). After the PRP samples were centrifuged at 250 g for 15 min to obtain platelet pellet and then washed with PBS (calcium-free, magnesium-free, and phenol red-free; Gibco; USA) three times. The PRP suspension was activated with 1 mL of 10 % CaCl2 and 1000 U thrombin (Hunan Yige Pharmaceutical, China), and then centrifuged in series at low speeds (300 g for 10 min, 2000g for 10 min) to discard cell debris. Then, the supernatant was filtered through a 0.22 μm filter (Millipore, Germany), and ultrafiltered under 4000 g centrifugation for 1 h. After repeating the ultrafiltration, the ultrafiltered liquid was transferred onto a 30 % sucrose/D2O cushion in an Ultra-Clear™ tube (Beckman Coulter, USA) and ultracentrifuged at 100,000 g for 70 min to pellet the exosomes. After washing the pelleted exosomes with PBS, exosome suspension was ultracentrifuged again at 100,000 g for 70 min. After washing the pelleted exosomes with PBS, the isolated exosomes were carefully resuspended in sterile PBS and stored at −80 °C for subsequent experiments.

The size distribution, morphology appearance, and specific exosome markers (CD63, CD81, and TSG101) were analyzed to identify the isolated exosomes. After the platelets were activated, the bioactive molecules in the platelets were released absolutely, thus these A-PLTs were selected as control. The cargoes in these isolated exosomes and A-PLT were analyzed using Bio-Plex Pro Human Cytokine 27-plex Assay kit (Bio-Plex, USA) and human angiogenic factors arrays (Raybiotech, USA).

4.6. Determining the minimum effective concentration of PLT-Exos encapsulation

Based on the results of rheological and biodegradative properties, the ADMMA pre-gels were made by dissolvable 5 % (w/v) ADMMA powders in sterile PBS along with 0.05 % (w/v) of photoinitiator (Irgacure 2959, Aladdin, CHN). To determine the minimum effective concentration of PLT-Exos encapsulation, four PLT-Exos@ADMMA-GELs were prepared with four gradient concentrations of PLT-Exos (0, 100, 200, 400 μg/mL), referenced in the human clinical trial [56], and the cytocompatibility, proliferation, migration, and tube formation of HUVECs (OriCell®, China, HUVEC-20001) were evaluated under the influence of the four PLT-Exos@ADMMA-GELs.

A live/dead cell staining kit (Abbkine, China, KTA1001) was used to illustrate the influence of the four hydrogels on HUVECs cytocompatibility. Briefly, the four hydrogels (200μL) in sol state were respectively injected into the upper chamber of a 24-well transwell chamber (Servicebio, China, WG3422) (n = 4), and placed into ultraviolet light to gel. After the upper chamber was immersed into the culture medium of HUVECs for 24 h, 2×10^4 HUVECs were seeded into the lower chamber. After incubating for 3 days, the cells were stained with a live/dead cell staining kit, and imaged by a fluorescent microscope (ApoTome 2, Carl Zeiss, Germany).

CCK-8 assay (Abbkine, China, KTA1001) was used to evaluate the influence of the four hydrogels on HUVECs proliferation. Briefly, the four hydrogels (200μL) in sol state were respectively injected into the upper chamber of a 24-well transwell chamber (n = 4), and placed into ultraviolet light to gel. After the upper chamber was immersed into the culture medium of HUVECs for 24 h, 2×10^4 HUVECs were seeded into the lower chamber. After incubating for 1, 3, 5, 7, 9, and 11 days, CCK-8 solution was added into each well and incubated for 2 h. The optical density (OD) was detected by a microplate absorbance reader (Tecan, Switzerland, M1000) at 450 nm.

A transwell migration assay was performed to evaluate the influence of the four hydrogels on HUVEC migration. Briefly, the four hydrogels (200μL) in sol state were respectively injected into the lower chamber of a 24-well transwell chamber (n = 4), placed into ultraviolet light to gel, and 600 μL culture medium of HUVECs was added into the lower chamber for 24 h. Then, 5×10^4 HUVECs were resuspended with an FBS-

free medium and added into the upper chamber. After incubating for 6 h, the transwell inserts were removed and rinsed gently with PBS, and those noninvaded cells on the surface of the microporous membrane were gently wiped off with a cotton swab. After fixation in 4 % paraformaldehyde (Biosharp, China, BL539A) for 10 min at room temperature, 0.1 % crystal violet (Servicebio, China, G1014) was used to stain for 5 min. Photographs were taken by microscopy (Leica, Germany, DMI3000B).

Tubular network formation of HUVECs was performed to further evaluate the angiogenic potential of the four PLT-Exos@ADMMA-GELs. Briefly, the four hydrogels (200μL) in sol state were respectively injected into the upper chamber of a 24-well transwell chamber, and placed into ultraviolet light to gel. After the upper chamber was immersed into the culture medium of HUVECs for 24 h, the down chamber was covered with 200uL matrix gel (Corning, America, 354248) for 30 min at 37 °C, and then seeded with 1.5 × 10^5/well of HUVECs (n = 4). After 6 h, HUVECs were taken by microscopy (Leica, Germany, DMI3000B) to count the number of lattice-like shapes.

4.7. Fabrication, appearance, and mechanical evaluation of PLT-Exos@ADMMA-MN

A self-designed PDMS mold (Fig. S2) was applied for preparing PLT-Exos@ADMMA-MN. Briefly, the PLT-Exos at a concentration of 200 μg/mL were mixed within an ADMMA pre-gel (5 %, w/v), and then deposited into the needle cavities of PDMS mold, and then kept under vacuum for 1 h to remove air bubbles at the bottom of the mold. Subsequently, the PDMS mold containing PLT-Exos@ADMMA pre-gel was exposed to UV light for gel. After keeping the mold in the dark for 24 h to dry the perfused PLT-Exos@ADMMA-GEL at room temperature, our MN was de-molded and stored under dry conditions at 4 °C before further use. The gross images of PLT-Exos@ADMMA-MN were captured for appearance observation. The surface morphology of PLT-Exos@ADMMA-MN was observed by SEM.

The mechanical properties of the PLT-Exos@ADMMA-MN were measured using a universal testing machine. The microneedle patch was fixed on the universal testing machine with the tips facing upward, with the breaking strength of the needle tip was measured at a test speed of 5 mm/min.

4.8. In-vitro release assay of PLT-Exos from PLT-Exos@ADMMA-MN

To detect the release profile of PLT-Exos from our MN, the PLT-Exos were labeled by the red fluorescence dye (Dil, D282, Invitrogen, USA) before being encapsulated into the ADMMA pre-gel. The Dil-labeled PLT-Exos@ADMMA-MN were immersed in PBS at 37 °C, and fluorescence images of the tips of Dil-labeled PLT-Exos@ADMMA-MN were captured by CLSM at day 0, 4, 7, 10, and 14. The fluorescence images of the tips of Dil-labeled PLT-Exos@ADMMA-MN at day 0 were taken to visualize the PLT-Exos distribution in the PLT-Exos@ADMMA-MN. In addition, the release rate of PLT-Exos was calculated by the following formula: $R=(D0-D_x)/D_0*100$ %. where "R" is the release rate, D_0 refers to the area of red fluorescence at day 0; and D_x refers to the area of red fluorescence at day 0, 4, 7, 10, or 14, respectively.

4.9. In-vitro immunomodulation and angiogenesis of PLT-Exos@ADMMA-MN

4.9.1. Cell culture systems

The immunomodulatory properties of PLT-Exos@ADMMA-MN were evaluated using a co-culture system of THP-1 macrophages and PLT-Exos@ADMMA-MN. Briefly, 200uL of PLT-Exos@ADMMA pre-gel was respectively injected into the upper chamber of a 24-well transwell chamber (n = 4), and placed into ultraviolet light to gel. The PLT-Exos@ADMMA-GEL on the plate was dried in a sterile and dark environment for 24 h at room temperature as MN for cell culture. To obtain THP-1 macrophages, THP-1 monocytes (ATCC TIB202, Manassas, VA) were cultured on the medium containing PMA (20 ng/mL, Sigma-Aldrich). After 24 h of incubation, these cells adhering to the Petri dish surface were THP-1 macrophages, which were collected and seeded into the lower chamber at a density of 5 × 10^5/well. THP-1 macrophages cultured within a medium containing lipopolysaccharide (LPS) (100 ng/mL, Solarbio, China) were set up as an LPS group. THP-1 macrophages cultured without LPS were set up as a CTL group. THP-1 macrophages cultured with an upper chamber loading PLT-Exos@ADMMA-MN were set up as an MN group.

The pro-angiogenic capacities of PLT-Exos@ADMMA-MN were evaluated using a co-culture system of HUVECs and PLT-Exos@ADMMA-MN. Briefly, 200uL of PLT-Exos@ADMMA pre-gel was respectively injected into the upper chamber of a 24-well transwell chamber (n = 4), and placed into ultraviolet light to gel. The PLT-Exos@ADMMA-GEL on the plate was dried in a sterile and dark environment for 24 h at room temperature as MN for cell culture. Then, 1.5 × 10^5/well of HUVECs were seeded into the lower chamber at a density of 5 × 10^5/well. HUVECs cultured within a medium containing VEGFα (100 ng/mL, Procell, CHN) were set up as a VEGF group. HUVECs cultured within a medium containing without VEGFα were set up as a CTL group. HUVECs cultured with an upper chamber loading PLT-Exos@ADMMA-MN were set up as MN group.

4.9.2. PLT-Exos uptake by THP-1 macrophages or HUVECs

PLT-Exos were labeled by the red fluorescence dye (Dil) before being encapsulated into the ADMMA pre-gel, the medium of THP-1 macrophages or HUVECs was incubated into this Dil-labeled PLT-Exos@ADMMA-MN for 24 h. The two mediums containing Dil-labeled PLT-Exos were respectively collected for culturing THP-1 macrophages or HUVECs. After 6 h of culture, the THP-1 macrophages or the HUVECs were stained by DAPI and anti-phalloidin and then captured by a fluorescence microscope for observing PLT-Exos uptake.

4.9.3. Flow cytometry

After 3 days of co-culture, the THP-1 macrophages were collected for flow cytometry using a flow cytometer (CyAN ADP, Beckman, USA). According to the sorting procedures (Fig. S4), three surface markers were used together to measure the counts of M1 macrophages (CD11b + CD206-$CD80^+$) and M2 macrophages (CD11b + CD206+$CD80^-$) by a subsequent flow-cytometry-activated cell sorting (FACS) gating scheme.

4.9.4. qRT-PCR

qRT-PCR was used to detect the expression of M1 macrophages related genes (CD80, INOS) and M2 macrophages related genes (CD206, CD163). Briefly, the collected THP-1 macrophages were used to extract total RNA with TRIzol reagent (CW Biotech, China), and cDNA was synthesized using a reverse transcription kit (Takara, Japan). cDNA was then amplified by qPCR system, all in 20 μL of the final reaction mixture. GAPDH was used as a reference for data processing. The primer sequences are shown in Table S2.

4.9.5. Enzyme-linked immunosorbent assays (ELISAs)

Using a co-culture system of THP-1 macrophages and PLT-Exos@ADMMA-MN, the cell supernatant on day 3 was collected for measuring TNF-α, IL-6, IL-10, IL-4, VEGFα, and PDGFββ content according to the instructions of the ELISA kit. The detailed information on the ELISA kits is listed in Table S1.

4.9.6. RNA sequencing and analysis

On day 3 of culture, the THP-1 macrophages in the CTL group or the MN group were collected for transcriptome analysis. Briefly, total RNA was extracted using Trizol reagent (Invitrogen, USA) from THP-1 macrophages in the CTL group or the MN group. The obtained RNA samples were sent to HaploX Genomics Center (Shenzhen, China) for RNA sequencing. The expression FPKM value of the respective gene in each

sample was determined using featureCounts software. Differential expression analysis was performed using DESeq software and counted using the DESeq algorithm. The genes with significantly different expressions were identified as follows: [log 2fold change] > 1 and P < 0.05. CIBERSORT was used to characterize the immune cell subsets in the CTL group or the MN group based on their gene expression profiles [61]. Through the GO (Gene ontology) analysis, the biological functions of differential genes were described, which included biological processes (BP), molecular function (MF), and cellular components (CC). The pathways with significant enrichment of differential genes were described by KEGG (Kyoto Encyclopedia of Genes and Genome) pathway enrichment analysis and GSEA (Gene Set Enrichment Analysis) dataset analysis.

4.9.7. CCK-8 assay

CCK-8 assay was used to evaluate the influence of our PLT-Exos@ADMMA-MN on HUVEC proliferation. After incubating for 1, 3, and 7 days, CCK-8 solution was added into each well and incubated for 2 h. The optical density (OD) was detected by a microplate absorbance reader at 450 nm.

4.9.8. Cell scratch test

A cell scratch test was performed to evaluate the influence of our PLT-Exos@ADMMA-MN on HUVEC migration. Briefly, when the density of the HUVECs proliferates to about 95 %, a straight line is drawn to create a uniform scratch with a 1-mL pipette tip. After incubating for 12 h, photographs were taken by microscopy (Leica, Germany, DMI3000B).

4.9.9. Tubular network formation

Tubular network formation of HUVECs was used to evaluate the pro-angiogenic potential of our PLT-Exos@ADMMA-MN. Briefly, after culturing for 6 h, HUVECs were taken by microscopy (Leica, Germany, DMI3000B) to measure the number of lattice-like shapes.

4.10. Animal experiment

4.10.1. Animal model of diabetic wound (DW)

Male Sprague Dawley rats were induced into diabetes by a single intraperitoneal injection of streptozotocin (90 mg/kg). The rats with stable high levels of blood glucose (300 mg/dl) for 2 weeks were used for the following experiments. These diabetic rats were randomly allocated into the ID, TO, or MN group, and then anesthetized by isoflurane gas. After the rats were shaved and sterilized, round full-thickness skin defects with a diameter of 2 cm were created on the back of each rat. The rats in the ID group were treated by intradermal (ID) injection of PLT-Exos solution, while in the TO group, the DW on the rat back was treated by topical administration (TO) of PLT-Exos@ADMMA-GEL. The rats in the MN group were treated by microneedles (MN) administration of PLT-Exos@ADMMA-MN.

4.10.2. PLT-Exos@ADMMA-MN capable of transdermal and sustained delivery of PLT-Exos

To evaluate the transdermal and sustained delivery of PLT-Exos of our MN, we prepared Dil-labeled PLT-Exos@ADMMA-MN or Dil-labeled PLT-Exos@ADMMA-GEL. The DW tissue was harvested 30 min or 7 days after treatment with topical administration of Dil-labeled PLT-Exos@ADMMA-GEL (TO group, the same PLT-Exos in our MN) or microneedles administration of Dil-labeled PLT-Exos@ADMMA-MN (MN group). The excised tissue was washed with deionized water, fixed with a 4 % formalin solution, and sectioned for the observation of Dil-positive red fluorescence using a fluorescent microscope. Additionally, after the rat DW was treated with intradermal injection of Dil-labeled PLT-Exos (ID group, the same PLT-Exos in our MN, n = 4) or microneedles administration of Dil-labeled PLT-Exos@ADMMA-MN (MN group, n = 4), whole-body fluorescence images were captured using in vivo imaging system (IVIS) (Lumina XR, PerkinElmer, Waltham, MA, USA), and the fluorescence intensity was comparatively measured in the DW region using the Living Image software for evaluating the sustained delivery of PLT-Exos of our MN.

4.10.3. Wound healing assay

The images of rat DWs at days 0, 7, 14, and 21 were imported into Image-Pro Plus (version 6.0.0; Media Cybernetics Inc.) for the calculation of wound closure by two investigators (Yanpeng Cao and Liang Liu). The percentage of wound closure was calculated as follows: (A0-At)/A0*100 %, where “A0” indicates the area of the original wound, and “At” is the area of the wound at the measured time point.

4.10.4. H&E and MT staining

At day 21, all rats were euthanized, and the wound tissues were harvested and fixed with 4 % paraformaldehyde. Then the tissues were embedded in paraffin and sectioned for H&E staining and MT staining to study the re-epithelialization and collagen deposition of wounds (n = 6 per group). In the H&E-stained sections, the percentage of re-epithelialization (E%) was calculated according to previously described methods: E% = Wt/Wo*100, where “Wo” is the length of the original wound, and “Wt” is the length of the neo-epithelium across the surface of the wound. In the MT-stained sections, the collagen deposition was calculated by detecting the mean staining intensity for Masson using Image-Pro Plus 6 software.

4.10.5. Immunofluorescent staining

On days 3 and 7, wound samples from each group were used to observe the macrophage polarization of DW. On days 7 and 14, wound samples from each group were used to detect angiogenesis that occurred in the granulation tissue of DW. The sections of harvested wound tissues were blocked with 1 % Bovine Serum Albumin (Aladdin, CHN) for 1 h and permeabilized with 2 % Triton X-100 for 30 min. After the sections were incubated with primary antibodies overnight at 4 °C, Alexa Fluor 488 or Alexa Fluor 594 conjugated secondary antibodies were used to stain these sections for 1 h at room temperature. Finally, these sections were counterstained with DAPI. The images were captured by a fluorescent microscope. Primary antibodies were listed as follows: anti-CD86 antibody (1:200, Abcam, USA), anti-CD206 antibody (1:200, Abcam, USA), anti-CD 31 antibody (1:200, Abcam, USA), anti-αSMA antibody (1:200, Abcam, USA).

4.10.6. Enzyme-linked immunosorbent assays (ELISA)

On days 3 and 7, the skin tissue acquired from the rat DW site was dissected for ELISA. Briefly, the specimen was immediately frozen in liquid nitrogen after dissection and then crushed into a fine powder using a precooled Bio-Pulverizer (BioSpecs, Bartlesville, OK, USA). The powdered tissue was extracted and centrifuged to collect the clear tissue extract. Protein concentration in the extract was determined using a Pierce BCA protein assay kit (Thermo Fisher Scientific Inc, Rockford, IL, USA). After that, rat ELISA kits for TNF-α, IL-6, IL-10, and IL-4 (Table S1) were used to measure protein levels. Concentrations of TNF-α, IL-6, IL-10, and IL-4 were normalized to total protein concentrations determined using the Pierce BCA protein assay.

4.10.7. Angiography

To evaluate angiogenesis in the DW healing process, experimental rats were perfused by Microfil (Microfil MV-122; Flow Tech, USA) on days 7 and 14 according to a previous study [28]. In brief, after anesthesia with 4 % chloral hydrate, the thoracic cavity was opened and the infusion needle was placed into the left ventricular. Heparinized normal saline, 10 % formalin, and 10 mL mixed microfil solution were perfused successively. After the contrast agent was fully polymerized, the skin of the DW was harvested and scanned by micro-CT (SKYSCAN 1176, Bruker, Kontich, Belgium) to quantify the angiogenesis in the DW site. Then, 3D reconstructions were generated with the application of the CTVol software (Skyscan Company). Parameter of the angiogenesis,

including vessel volume/tissue volume (%) and vessel diameter (μm), was analyzed using the CTAn software (Skyscan Company).

4.11. Statistical analysis

Data were collected and documented as mean ± standard deviation, and the data were statistically analyzed using GraphPad Prism 9.0 software. One-way ANOVA was used for comparison between different groups, while a student t-test was utilized to compare the statistical difference between the two groups. Statistical difference was labeled in parallel, and * indicates $p < 0.0332$, which is considered a statistically significant difference, while ** indicates $p < 0.0021$, *** indicates $p < 0.0002$, **** indicates $p < 0.0001$, and "ns" indicates no significance.

Data availability statement

The data are available from the corresponding author upon reasonable request.

Conflicts of interest

The authors declared no conflict of interest about the publication of this paper.

Funding declaration

This work was financially supported through grants from the National Natural Science Foundation of China (Grant No.82272497), Hunan Provincial Natural Science Foundation (Grant Nos. 2021JJ20093, 2022JJ30001, 2023JJ40090), the Hunan Provincial Health Commission Scientific Research Projects (Grant No.202204075237).

Ethics approval and consent to participate

The Ethics Committee of Chenzhou No. 1 People's Hospital approved the experimental procedures for the use of male SD rats (3 months old) and the collection of human blood for PLT-Exos isolation (No. 2023001).

CRediT authorship contribution statement

Yanpeng Cao: Writing – original draft, Visualization, Validation, Software, Methodology, Investigation, Funding acquisition, Formal analysis, Data curation, Conceptualization. **Bei Chen:** Writing – original draft, Visualization, Validation, Resources, Methodology, Investigation, Formal analysis, Data curation, Conceptualization. **Qixing Liu:** Software, Resources, Investigation, Formal analysis. **Yiyang Mao:** Methodology, Investigation, Formal analysis, Data curation. **Yusheng He:** Validation, Resources, Methodology, Formal analysis. **Xiaoren Liu:** Supervision, Resources, Formal analysis. **Xin Zhao:** Methodology, Investigation, Data curation. **Yaowu Chen:** Resources, Formal analysis. **Xiying Li:** Validation, Project administration. **Yabei Li:** Investigation, Formal analysis. **Liang Liu:** Methodology, Data curation. **Chengwu Guo:** Software. **Shiyu Liu:** Validation. **Fenghua Tan:** Visualization. **Hongbin Lu:** Writing – review & editing, Supervision. **Jun Liu:** Writing – review & editing, Supervision, Resources, Project administration, Funding acquisition, Conceptualization. **Can Chen:** Writing – review & editing, Writing – original draft, Supervision, Project administration, Funding acquisition, Conceptualization.

Declaration of competing interest

The authors declare that they have no known competing financial interests or personal relationships that could have appeared to influence the work reported in this paper.

Appendix A. Supplementary data

Supplementary data to this article can be found online at https://doi.org/10.1016/j.bioactmat.2024.08.016.

References

[1] N.H. Cho, J.E. Shaw, S. Karuranga, Y. Huang, J.D. da Rocha Fernandes, A. W. Ohlrogge, B. Malanda, IDF Diabetes Atlas: global estimates of diabetes prevalence for 2017 and projections for 2045, Diabetes Res. Clin. Pract. 138 (2018) 271–281.
[2] K. Ogurtsova, J.D. da Rocha Fernandes, Y. Huang, U. Linnenkamp, L. Guariguata, N.H. Cho, D. Cavan, J.E. Shaw, L.E. Makaroff, IDF Diabetes Atlas: global estimates for the prevalence of diabetes for 2015 and 2040, Diabetes Res. Clin. Pract. 128 (2017) 40–50.
[3] J.E. Shaw, R.A. Sicree, P.Z. Zimmet, Global estimates of the prevalence of diabetes for 2010 and 2030, Diabetes Res. Clin. Pract. 87 (1) (2010) 4–14.
[4] H. Liu, H. Liu, X. Deng, M. Chen, X. Han, W. Yan, N. Wang, CXCR4 antagonist delivery on decellularized skin scaffold facilitates impaired wound healing in diabetic mice by increasing expression of SDF-1 and enhancing migration of CXCR4-positive cells, Wound Repair Regen. 25 (4) (2017) 652–664.
[5] C. Shrestha, L. Zhao, K. Chen, H. He, Z. Mo, Enhanced healing of diabetic wounds by subcutaneous administration of human umbilical cord derived stem cells and their conditioned media, Internet J. Endocrinol. 2013 (2013) 592454.
[6] A.E. Louiselle, S.M. Niemiec, C. Zgheib, K.W. Liechty, Macrophage polarization and diabetic wound healing, Transl. Res. 236 (2021) 109–116.
[7] Y. Qian, Y. Zheng, J. Jin, X. Wu, K. Xu, M. Dai, Q. Niu, H. Zheng, X. He, J. Shen, Immunoregulation in diabetic wound repair with a photoenhanced glycyrrhizic acid hydrogel scaffold, Adv. Mater. 34 (29) (2022) e2200521.
[8] S. Zhu, B. Zhao, M. Li, H. Wang, J. Zhu, Q. Li, H. Gao, Q. Feng, X. Cao, Microenvironment responsive nanocomposite hydrogel with NIR photothermal therapy, vascularization and anti-inflammation for diabetic infected wound healing, Bioact. Mater. 26 (2023) 306–320.
[9] N. Hu, Z. Cai, X. Jiang, C. Wang, T. Tang, T. Xu, H. Chen, X. Li, X. Du, W. Cui, Hypoxia-pretreated ADSC-derived exosome-embedded hydrogels promote angiogenesis and accelerate diabetic wound healing, Acta Biomater. 157 (2023) 175–186.
[10] Y. Xiong, Z. Lin, P. Bu, T. Yu, Y. Endo, W. Zhou, Y. Sun, F. Cao, G. Dai, Y. Hu, L. Lu, L. Chen, P. Cheng, K. Zha, M.A. Shahbazi, Q. Feng, B. Mi, G. Liu, A whole-course-repair system based on neurogenesis-angiogenesis crosstalk and macrophage reprogramming promotes diabetic wound healing, Adv. Mater. 35 (19) (2023) e2212300.
[11] Y. Xiong, B.B. Mi, Z. Lin, Y.Q. Hu, L. Yu, K.K. Zha, A.C. Panayi, T. Yu, L. Chen, Z. P. Liu, A. Patel, Q. Feng, S.H. Zhou, G.H. Liu, The role of the immune microenvironment in bone, cartilage, and soft tissue regeneration: from mechanism to therapeutic opportunity, Mil Med Res 9 (1) (2022) 65.
[12] A.J. Boulton, L. Vileikyte, G. Ragnarson-Tennvall, J. Apelqvist, The global burden of diabetic foot disease, Lancet 366 (9498) (2005) 1719–1724.
[13] Y. Liang, X. Zhao, T. Hu, B. Chen, Z. Yin, P.X. Ma, B. Guo, Adhesive hemostatic conducting injectable composite hydrogels with sustained drug release and photothermal antibacterial activity to promote full-thickness skin regeneration during wound healing, Small 15 (12) (2019) e1900046.
[14] M. Wu, Z. Lu, K. Wu, C. Nam, L. Zhang, J. Guo, Recent advances in the development of nitric oxide-releasing biomaterials and their application potentials in chronic wound healing, J. Mater. Chem. B 9 (35) (2021) 7063–7075.
[15] H.S. Kim, X. Sun, J.H. Lee, H.W. Kim, X. Fu, K.W. Leong, Advanced drug delivery systems and artificial skin grafts for skin wound healing, Adv. Drug Deliv. Rev. 146 (2019) 209–239.
[16] N. Mandakhbayar, Y. Ji, A. El-Fiqi, K.D. Patel, D.S. Yoon, K. Dashnyam, O. Bayaraa, G. Jin, K. Tsogtbaatar, T.H. Kim, J.H. Lee, H.W. Kim, Double hits with bioactive nanozyme based on cobalt-doped nanoglass for acute and diabetic wound therapies through anti-inflammatory and pro-angiogenic functions, Bioact. Mater. 31 (2024) 298–311.
[17] H. Yu, Y. Li, Y. Pan, H. Wang, W. Wang, X. Ren, H. Yuan, Z. Lv, Y. Zuo, Z. Liu, W. Lin, Q. Yao, Multifunctional porous poly (L-lactic acid) nanofiber membranes with enhanced anti-inflammation, angiogenesis and antibacterial properties for diabetic wound healing, J. Nanobiotechnol. 21 (1) (2023) 110.
[18] S. Lyu, Z. Dong, X. Xu, H.P. Bei, H.Y. Yuen, C.W. James Cheung, M.S. Wong, Y. He, X. Zhao, Going below and beyond the surface: microneedle structure, materials, drugs, fabrication, and applications for wound healing and tissue regeneration, Bioact. Mater. 27 (2023) 303–326.
[19] P. Jiang, Q. Li, Y. Luo, F. Luo, Q. Che, Z. Lu, S. Yang, Y. Yang, X. Chen, Y. Cai, Current status and progress in research on dressing management for diabetic foot ulcer, Front. Endocrinol. 14 (2023) 1221705.
[20] X. Zhang, Y. Wang, J. Chi, Y. Zhao, Smart Microneedles for Therapy and Diagnosis, vol. 2020, Research (Wash D C), 2020 7462915.
[21] R. Mo, H. Zhang, Y. Xu, X. Wu, S. Wang, Z. Dong, Y. Xia, D. Zheng, Q. Tan, Transdermal drug delivery via microneedles to mediate wound microenvironment, Adv. Drug Deliv. Rev. 195 (2023) 114753.
[22] V.D. Bui, S. Son, W. Xavier, V.Q. Nguyen, J.M. Jung, J. Lee, S. Shin, W. Um, J. Y. An, C.H. Kim, Y. Song, Y. Li, J.H. Park, Dissolving microneedles for long-term storage and transdermal delivery of extracellular vesicles, Biomaterials 287 (2022) 121644.

[23] X. Yu, J. Zhao, D. Fan, The progress in the application of dissolving microneedles in biomedicine, Polymers 15 (20) (2023).
[24] D.J. Wainwright, Use of an acellular allograft dermal matrix (AlloDerm) in the management of full-thickness burns, Burns 21 (4) (1995) 243–248.
[25] B. Buinewicz, B. Rosen, Acellular cadaveric dermis (AlloDerm): a new alternative for abdominal hernia repair, Ann. Plast. Surg. 52 (2) (2004) 188–194.
[26] R.S. Kirsner, G. Bohn, V.R. Driver, J.L. Mills Sr., L.B. Nanney, M.L. Williams, S. C. Wu, Human acellular dermal wound matrix: evidence and experience, Int. Wound J. 12 (6) (2015) 646–654.
[27] R. Yu, H. Zhang, B. Guo, Conductive biomaterials as bioactive wound dressing for wound healing and skin tissue engineering, Nano-Micro Lett. 14 (1) (2021) 1.
[28] Y. Yu, H. Xiao, G. Tang, H. Wang, J. Shen, Y. Sun, S. Wang, W. Kong, Y. Chai, X. Liu, X. Wang, G. Wen, Biomimetic hydrogel derived from decellularized dermal matrix facilitates skin wounds healing, Mater Today Bio 21 (2023) 100725.
[29] R. Kalluri, V.S. LeBleu, The biology, function, and biomedical applications of exosomes, Science (New York, N.Y.) 367 (6478) (2020).
[30] X.C. Jiang, T. Zhang, J.Q. Gao, The in vivo fate and targeting engineering of crossover vesicle-based gene delivery system, Adv. Drug Deliv. Rev. 187 (2022) 114324.
[31] L. Yang, K.D. Patel, C. Rathnam, R. Thangam, Y. Hou, H. Kang, K.B. Lee, Harnessing the therapeutic potential of extracellular vesicles for biomedical applications using multifunctional magnetic nanomaterials, Small 18 (13) (2022) e2104783.
[32] J. Wu, Y. Piao, Q. Liu, X. Yang, Platelet-rich plasma-derived extracellular vesicles: a superior alternative in regenerative medicine? Cell Prolif. 54 (12) (2021) e13123.
[33] T. Spakova, J. Janockova, J. Rosocha, Characterization and therapeutic use of extracellular vesicles derived from platelets, Int. J. Mol. Sci. 22 (18) (2021).
[34] J. Johnson, Y.W. Wu, C. Blyth, G. Lichtfuss, H. Goubran, T. Burnouf, Prospective therapeutic applications of platelet extracellular vesicles, Trends Biotechnol. 39 (6) (2021) 598–612.
[35] M. Saumell-Esnaola, D. Delgado, G. Garcia Del Cano, M. Beitia, J. Salles, I. Gonzalez-Burguera, P. Sanchez, M. Lopez de Jesus, S. Barrondo, M. Sanchez, Isolation of platelet-derived exosomes from human platelet-rich plasma: biochemical and morphological characterization, Int. J. Mol. Sci. 23 (5) (2022).
[36] S. Patel, K. Ziai, J.G. Lighthall, S.G. Walen, Biologics and acellular dermal matrices in head and neck reconstruction: a comprehensive review, Am. J. Otolaryngol. 43 (1) (2022) 103233.
[37] X. Guo, D. Mu, F. Gao, Efficacy and safety of acellular dermal matrix in diabetic foot ulcer treatment: a systematic review and meta-analysis, Int. J. Surg. 40 (2017) 1–7.
[38] A. Esmaeili, E. Biazar, M. Ebrahimi, S. Heidari Keshel, B. Kheilnezhad, F. Saeedi Landi, Acellular fish skin for wound healing, Int. Wound J. 20 (7) (2023) 2924–2941.
[39] E.Z. DeSagun, J.L. Botts, A. Srivastava, M. Hanumadass, R.J. Walter, Long-term outcome of xenogenic dermal matrix implantation in immunocompetent rats, J. Surg. Res. 96 (1) (2001) 96–106.
[40] A. Srivastava, E.Z. DeSagun, L.J. Jennings, S. Sethi, A. Phuangsab, M. Hanumadass, H.M. Reyes, R.J. Walter, Use of porcine acellular dermal matrix as a dermal substitute in rats, Ann. Surg. 233 (3) (2001) 400–408.
[41] C.W. Lin, C.M. Hung, W.J. Chen, J.C. Chen, W.Y. Huang, C.S. Lu, M.L. Kuo, S. G. Chen, New horizons of macrophage immunomodulation in the healing of diabetic foot ulcers, Pharmaceutics 14 (10) (2022).
[42] X. Zhang, X. Chen, H. Hong, R. Hu, J. Liu, C. Liu, Decellularized extracellular matrix scaffolds: recent trends and emerging strategies in tissue engineering, Bioact. Mater. 10 (2022) 15–31.
[43] E. García-Gareta, Y. Abduldaiem, P. Sawadkar, C. Kyriakidis, F. Lali, K.V. Greco, Decellularised scaffolds: just a framework? Current knowledge and future directions, J. Tissue Eng. 11 (2020) 2041731420942903.
[44] M.L. Pérez, C. Castells-Sala, P. López-Chicón, N. Nieto-Nicolau, A. Aiti, O. Fariñas, R.P. Casaroli-Marano, O. Porta, A. Vilarrodona, Fast protocol for the processing of split-thickness skin into decellularized human dermal matrix, Tissue Cell 72 (2021) 101572.
[45] C.G. Williams, A.N. Malik, T.K. Kim, P.N. Manson, J.H. Elisseeff, Variable cytocompatibility of six cell lines with photoinitiators used for polymerizing hydrogels and cell encapsulation, Biomaterials 26 (11) (2005) 1211–1218.
[46] H. Xiao, X. Chen, X. Liu, G. Wen, Y. Yu, Recent advances in decellularized biomaterials for wound healing, Mater Today Bio 19 (2023) 100589.
[47] Q. Li, W. Hu, Q. Huang, J. Yang, B. Li, K. Ma, Q. Wei, Y. Wang, J. Su, M. Sun, S. Cui, R. Yang, H. Li, X. Fu, C. Zhang, MiR146a-loaded engineered exosomes released from silk fibroin patch promote diabetic wound healing by targeting IRAK1, Signal Transduct. Targeted Ther. 8 (1) (2023) 62.
[48] H.P. Bei, P.M. Hung, H.L. Yeung, S. Wang, X. Zhao, Bone-a-Petite: engineering exosomes towards bone, osteochondral, and cartilage repair, Small 17 (50) (2021) e2101741.
[49] S. Lu, L. Lu, Y. Liu, Z. Li, Y. Fang, Z. Chen, J. Zhou, Native and engineered extracellular vesicles for wound healing, Front. Bioeng. Biotechnol. 10 (2022) 1053217.
[50] L. Yu, J. Qin, J. Xing, Z. Dai, T. Zhang, F. Wang, J. Zhou, X. Zhang, X. Chen, Y. Gu, The mechanisms of exosomes in diabetic foot ulcers healing: a detailed review, J. Mol. Med. (Berl.) 101 (10) (2023) 1209–1228.
[51] M.A. Tienda-Vazquez, J.M. Hanel, E.M. Marquez-Arteaga, A.P. Salgado-Alvarez, C. Q. Scheckhuber, J.R. Alanis-Gomez, J.I. Espinoza-Silva, M. Ramos-Kuri, F. Hernandez-Rosas, E.M. Melchor-Martinez, R. Parra-Saldivar, Exosomes: a promising strategy for repair, regeneration and treatment of skin disorders, Cells 12 (12) (2023).
[52] J. Feng, Y. Yao, Q. Wang, X. Han, X. Deng, Y. Cao, X. Chen, M. Zhou, C. Zhao, Exosomes: potential key players towards novel therapeutic options in diabetic wounds, Biomedicine & pharmacotherapy = Biomedecine & pharmacotherapie 166 (2023) 115297.
[53] W. Zhu, Y. Dong, P. Xu, Q. Pan, K. Jia, P. Jin, M. Zhou, Y. Xu, R. Guo, B. Cheng, A composite hydrogel containing resveratrol-laden nanoparticles and platelet-derived extracellular vesicles promotes wound healing in diabetic mice, Acta Biomater. 154 (2022) 212–230.
[54] Y. Zhang, X. Wang, J. Chen, D. Qian, P. Gao, T. Qin, T. Jiang, J. Yi, T. Xu, Y. Huang, Q. Wang, Z. Zhou, T. Bao, X. Zhao, H. Liu, Z. Zheng, J. Fan, S. Zhao, Q. Li, G. Yin, Exosomes derived from platelet-rich plasma administration in site mediate cartilage protection in subtalar osteoarthritis, J. Nanobiotechnol. 20 (1) (2022) 56.
[55] J. Qian, X. Wang, G. Su, X. Shu, Z. Huang, H. Jiang, Q. Zhu, Platelet-rich plasma-derived exosomes attenuate intervertebral disc degeneration by promoting NLRP3 autophagic degradation in macrophages, Int. Immunopharm. 110 (2022) 108962.
[56] J. Johnson, S.Q.K. Law, M. Shojaee, A.S. Hall, S. Bhuiyan, M.B.L. Lim, A. Silva, K.J. W. Kong, M. Schoppet, C. Blyth, H.N. Ranasinghe, N. Sejic, M.J. Chuei, O. C. Tatford, A. Cifuentes-Rius, P.F. James, A. Tester, I. Dixon, G. Lichtfuss, First-in-human clinical trial of allogeneic, platelet-derived extracellular vesicles as a potential therapeutic for delayed wound healing, J. Extracell. Vesicles 12 (7) (2023) e12332.
[57] T. Ning, F. Yang, D. Chen, Z. Jia, R. Yuan, Z. Du, S. Liu, Y. Yu, X. Dai, X. Niu, Y. Fan, Synergistically detachable microneedle dressing for programmed treatment of chronic wounds, Adv. Healthcare Mater. 11 (11) (2022) e2102180.
[58] A. Mantovani, S.K. Biswas, M.R. Galdiero, A. Sica, M. Locati, Macrophage plasticity and polarization in tissue repair and remodelling, J. Pathol. 229 (2) (2013) 176–185.
[59] S.Y. Kim, M.G. Nair, Macrophages in wound healing: activation and plasticity, Immunol. Cell Biol. 97 (3) (2019) 258–267.
[60] A.E. Boniakowski, A.S. Kimball, B.N. Jacobs, S.L. Kunkel, K.A. Gallagher, Macrophage-mediated inflammation in normal and diabetic wound healing, J. Immunol. 199 (1) (2017) 17–24.
[61] A.M. Newman, C.L. Liu, M.R. Green, A.J. Gentles, W. Feng, Y. Xu, C.D. Hoang, M. Diehn, A.A. Alizadeh, Robust enumeration of cell subsets from tissue expression profiles, Nat. Methods 12 (5) (2015) 453–457.
[62] J.M. Platnich, D.A. Muruve, NOD-like receptors and inflammasomes: a review of their canonical and non-canonical signaling pathways, Arch. Biochem. Biophys. 670 (2019) 4–14.
[63] S. Ryu, S. Sidorov, E. Ravussin, M. Artyomov, A. Iwasaki, A. Wang, V.D. Dixit, The matricellular protein SPARC induces inflammatory interferon-response in macrophages during aging, Immunity 55 (9) (2022) 1609–1626.e7.
[64] B. Ma, Y. Yang, Z. Li, D. Zhao, W. Zhang, Y. Jiang, D. Xue, Modular bioinformatics analysis demonstrates that a Toll-like receptor signaling pathway is involved in the regulation of macrophage polarization, Mol. Med. Rep. 18 (5) (2018) 4313–4320.
[65] R. Yu, C. Ma, G. Li, J. Xu, D. Feng, X. Lan, Inhibition of toll-like receptor 4 signaling pathway accelerates the repair of avascular necrosis of femoral epiphysis through regulating macrophage polarization in perthes disease, Tissue Eng Regen Med 20 (3) (2023) 489–501.
[66] A.P. Veith, K. Henderson, A. Spencer, A.D. Sligar, A.B. Baker, Therapeutic strategies for enhancing angiogenesis in wound healing, Adv. Drug Deliv. Rev. 146 (2019) 97–125.
[67] U.A. Okonkwo, L.A. DiPietro, Diabetes and wound angiogenesis, Int. J. Mol. Sci. 18 (7) (2017).
[68] X.L. Zhu, D.Y. Hu, Z.X. Zeng, W.W. Jiang, T.Y. Chen, T.C. Chen, W.Q. Liao, W. Z. Lei, W.J. Fang, W.H. Pan, XB130 inhibits healing of diabetic skin ulcers through the PI3K/Akt signalling pathway, World J. Diabetes 14 (9) (2023) 1369–1384.
[69] M. Monavarian, S. Kader, S. Moeinzadeh, E. Jabbari, Regenerative scar-free skin wound healing, Tissue Eng., Part B 25 (4) (2019) 294–311.
[70] M. Rodrigues, N. Kosaric, C.A. Bonham, G.C. Gurtner, Wound healing: a cellular perspective, Physiol. Rev. 99 (1) (2019) 665–706.
[71] M. Sharifiaghdam, E. Shaabani, R. Faridi-Majidi, S.C. De Smedt, K. Braeckmans, J. C. Fraire, Macrophages as a therapeutic target to promote diabetic wound healing, Mol. Ther. : the journal of the American Society of Gene Therapy 30 (9) (2022) 2891–2908.
[72] B. Zhang, Y. Su, J. Zhou, Y. Zheng, D. Zhu, Toward a better regeneration through implant-mediated immunomodulation: harnessing the immune responses, Adv. Sci. 8 (16) (2021) e2100446.
[73] T. Lazarov, S. Juarez-Carreño, N. Cox, F. Geissmann, Physiology and diseases of tissue-resident macrophages, Nature 618 (7966) (2023) 698–707.
[74] L.A. DiPietro, Angiogenesis and wound repair: when enough is enough, J. Leukoc. Biol. 100 (5) (2016) 979–984.
[75] Q. Li, Y. Xu, K. Lv, Y. Wang, Z. Zhong, C. Xiao, K. Zhu, C. Ni, K. Wang, M. Kong, X. Li, Y. Fan, F. Zhang, Q. Chen, Y. Li, Q. Li, C. Liu, J. Zhu, S. Zhong, J. Wang, Y. Chen, J. Zhao, D. Zhu, R. Wu, J. Chen, W. Zhu, H. Yu, R. Ardehali, J.J. Zhang, J. Wang, X. Hu, Small extracellular vesicles containing miR-486-5p promote angiogenesis after myocardial infarction in mice and nonhuman primates, Sci. Transl. Med. 13 (584) (2021).